Extreme-Ultraviolet Plasma Radiation Source with Wide-Angle Plasma Irradiation and Collection

Abstract

A variety of source collection mirror designs can provide an output beam with a wide collection angle and good uniformity, for an EUV lithography system using a laser-produced plasma source. The collection mirror can also perform the dual-use function of focusing wide-angle laser radiation onto the plasma as well as collecting EUV emission from the plasma.

Background

Extreme ultraviolet (EUV) lithography systems typically use a laser-produced plasma (LPP) source to generate EUV radiation; see FIG. 1. A high-power, pulsed laser beam **1.1** heats tin droplets to create an ionized plasma **1.2** and generate EUV radiation **1.3**, which is collected by an ellipsoidal mirror **1.4** and reflected through an intermediate focus (IF) **1.5**. (The laser beam transmits through a small aperture **1.6** in the center of mirror **1.4**.) Typically, two laser pulses are used: a short-wavelength pre-pulse to vaporize and expand the tin droplet, followed by a main pulse from a 10.6-micron CO_2 laser to create an ionized plasma. The plasma emission is peaked at an EUV wavelength of approximately 13.5 nm, and a multilayer mirror comprising alternating layers of silicon (Si) and molybdenum (Mo) is used to efficiently reflect 13.5-nm radiation. (This disclosure is focused primarily on a 13.5-nm wavelength, but the principles and mechanisms disclosed herein are equally applicable to other wavelengths and mirror types.)

The collection mirror geometry is illustrated in FIG. 2. The mirror **1.4** has rotational symmetry around an optical axis **2.1** going through the plasma **1.2** and IF **1.5**. Optical rays emitted from the plasma at axial collection angle θ are reflected through the IF at axial output angle θ'. The incidence angle α on the mirror is determined by θ and θ':

$$\theta = \theta' + 2\alpha \tag{1}$$

A limitation of Mo/Si mirrors is that they cannot reflect efficiently at incidence angles α between about 35º and 50º. FIG. 3 illustrates the typical reflection efficiency *R* of a Mo/Si mirror at wavelength 13.5 nm as a function of α, with the mirror design parameters optimized for each α value. (Appendix A details the mirror design assumed in FIG. 3.) The reflectance is polarization-dependent and is plotted separately for TE and TM polarizations (curves **3.1** and **3.2**, respectively). High efficiency can be obtained for TE polarization over all incidence angles, but the TM efficiency drops to zero at 42.7º (the Brewster angle for molybdenum).

EUV mirrors can be classified as "low-angle" or "high-angle" depending on whether they operate at incidence angles below or above 42.7º. (Low-angle mirrors are sometimes loosely characterized as "normal-incidence" or "near-normal-incidence" mirrors, and high-angle mirrors are sometimes termed "grazing-incidence" mirrors.) The collector illustrated in FIG. 2 is a low-angle mirror with maximum incidence angle α of 35º and maximum output angle θ' of 11.5º (based on a numerical aperture $\sin\theta' = 0.2$). This implies a maximum collection angle θ of 81.5º (from Eq. (1)). The total collection solid angle is 5.4 steradian, about 43% of the full 4π

spherical emission range. (These numerical values are only illustrative; they do not necessarily correspond exactly to an existing collector configuration.)

Mirror efficiency is one factor limiting collection efficiency, but even with 100% efficient mirrors an increased collection angle would be problematic because of extreme nonuniformity in the output beam's radiant intensity, defined as radiant flux per solid angle, i.e., watts per steradian, as a function of ray direction [1].

In the following discussion the term "intensity" will generally mean spectral radiant intensity, i.e. spectral intensity per unit wavelength interval (watts per steradian-nanometer) at wavelength 13.5 nm.

The optical geometry defining the output intensity is illustrated in FIG. 4. For a differential collection angle $d\theta$, rays emitted from the plasma **1.2** between axial collection angles θ and $\theta + d\theta$ (over all azimuth angles around axis **2.1**) cover an annular solid angle $d\Omega$ at the plasma, and are reflected through the IF **1.5** between output angles θ' and $\theta' + d\theta'$ covering an annular output solid angle $d\Omega'$ at the IF, where

$$d\Omega = 2\pi \sin\theta \, d\theta, \quad d\Omega' = 2\pi \sin\theta' \, d\theta' \tag{2}$$

The radiant power emitted over solid angle $d\Omega$ is $I \, d\Omega$, where I is the source intensity; and the output power over solid angle $d\Omega'$ is $I' \, d\Omega'$, where I' is the output intensity. The output power is the same as the input power, except for attenuation by the mirror reflectance R (averaged over TE and TM polarizations, at wavelength 13.5 nm),

$$I' \, d\Omega' = R \, I \, d\Omega \tag{3}$$

Hence, the output-to-source intensity ratio is

$$\frac{I'}{I} = R \frac{d\Omega}{d\Omega'} = R \frac{\sin\theta \, d\theta}{\sin\theta' \, d\theta'} \tag{4}$$

FIG. 5 shows a plot of I'/I as a function of θ' for the collector mirror of FIG. 2. Two cases are plotted: an ideal 100%-reflective mirror ($R = 1$, curve **5.1**), and an actual mirror as specified in Appendix A (curve **5.2**). Increasing the collection range beyond the 81.5° limit would make the output intensity more severely nonuniform.

A third factor that limits the practically achievable collection angle is the plasma's angular intensity profile. As illustrated in FIG. 1, the plasma is front-irradiated by the laser, and most of the generated EUV is emitted into the hemisphere facing the laser. (See Fig. 14 in [2].) There is comparatively little backside-emitted EUV (toward the IF), so extending the collection range significantly beyond the front-facing hemisphere would provide little benefit. The ionized tin atoms emit EUV isotropically, but the excessive tin mass absorbs forward-directed EUV and generates debris from incompletely vaporized tin.

Alternative EUV collection mirror designs

Some innovations have been made or proposed in the literature to at least partially overcome the above-outlined deficiencies of LPP collection systems. These innovations, along with some novel improvements on the published work, are outlined below.

U.S. Patent 7,405,871 [3], hereafter "'871", discloses an LPP collector system in the form of a mirror doublet comprising two annular, low-angle mirror elements (**402** and **406** in FIG. 4 of '871), which operate conjunctively to collect EUV radiation from a plasma source (**405**) and direct it in a forward direction. (In '871 FIG. 4 the laser would normally irradiate the plasma from the right side, and the "forward" direction is to the left.) '871 also illustrates an additional mirror **401** for collecting backward-emitted plasma radiation and directing it onto mirrors **402** and **406**, but this and other similar configurations illustrated in '871 appear to be impractical because the optical path between mirrors **401** and **402** is blocked by the plasma.

U.S. Patent 8,023,182 [4], hereafter "'182", similarly discloses the '871 doublet mirror ("**E1**", comprising elements **2** and **4** in '182 FIG'S. 1-4). There is no mirror to collect backward-emitted radiation (such as '871 element **401**) because '182 envisages the collector being used with a capillary discharge plasma **1** (described as a "very bulky device"), which only emits EUV into a forward-facing hemisphere. (FIG. 1 in '182 replicates the '871 FIG. 7 discharge-source embodiment, which also lacks element **401**.)

The '182 patent also discloses additional mirror doublets such as "**E2**" comprising mirror elements **7** and **9** in '182 FIG. 2. However, these doublets differ from the **E1** doublet adapted from '871. As illustrated in '182 FIG. 2, any optical ray traversing doublet **E1** crosses itself after reflecting from mirror **4** whereas the second mirror **9** in **E2** is "placed centrally" so that rays traversing **E2** do not cross themselves. A disadvantage of this configuration is that a portion of the source emission is blocked by the backside of a centrally located mirror (such as mirrors **9** and **13** in '182 FIG. 3 or mirror **17** in '182 FIG. 4).

Another type of collection mirror doublet comprises a low-angle element and a high-angle element, such as elements **302** and **310** in '871 FIG. 3. U.S. Patent 9,754,695 [5], hereafter '695, also discloses mirror doublets comprising low-angle and high-angle elements (e.g. elements **28** and **30** in '695 FIG. 2). The '695 doublet is further configured to generate an output beam of uniform intensity.

A novel LPP collection mirror design improving upon the published work is illustrated in FIG. 6A and enlarged views in FIG'S. 6B and 6C. The system comprises an ellipsoidal mirror **6.1** and a group **6.2** of low-angle mirror doublets labeled as **6.2.1** … **6.2.6** in FIG. 6B. Each doublet comprises two low-angle mirrors. For example, FIG. 6C shows doublet **6.2.1** comprising mirrors **6.2.1.1** and **6.2.1.2**, which are annular mirrors having rotational symmetry around the optical axis **2.2**. The mirrors in combination collect radiation from plasma source **1.2** over collection angles θ up to 155º, covering 95% of the full spherical emission range around the plasma. The mirrors could be designed to cover a larger or smaller range. The radiation is focused through the IF **1.5** over a range of output angles θ' up to 11.5º ($\sin\theta' \leq 0.2$), the same as FIG. 2. A typical ray **6.3** illustrates the collection and output angles θ and θ'.

The illustrated embodiment in FIG. 6A has six doublets. More or fewer doublets could be used, but a single doublet similar to that illustrated in '871 FIG. 4 and covering the full θ range up to 155º would be impractically large. The doublet mirrors are not "placed centrally" as described in '182, and there are no mirror backside blockages of the type illustrated in '182 FIG'S. 3 and 4.

The collection mirrors **6.2** illustrated in FIG'S. 6A-6C are designed to provide a uniform output intensity profile I', taking into account the mirror reflectance characteristics but assuming a uniform and isotropic source intensity I. The intensity ratio I'/I versus θ' is illustrated in FIG. 7 as curve **7.1**, compared to curve **5.2** from FIG. 5 (representing FIG. 2). The output intensity from the ellipsoid varies by a factor of 4.3 from center to edge for FIG. 2 (curve **5.2**) and by a factor of 4.9 for FIG. 6A (curve **7.1**). The flat outer portion of curve **7.1** corresponds to output radiation from the doublets **6.2**. ("+" marks on the curve demark angle ranges covered by different doublets.) The doublets are configured to maintain continuity of the output intensity across the boundary of mirror **6.1**. Appendix B outlines the mirror design methodology, which can be adapted to satisfy alternative design objectives, e.g. to take into account nonuniform source intensity or to provide a specified, nonuniform output intensity profile.

The ellipsoid **6.1** in FIG. 6A covers θ angles ranging up to 81.3º. This limit is determined to match the maximum incidence angles between the ellipsoid **6.1** and the doublet mirrors **6.2**. (The incidence angle is highest on element **6.2.1.2** and the maximum is 37.5º.) Reducing (or increasing) the ellipsoid θ limit would result in lower (higher) incidence angles on the ellipsoid and higher (lower) angles on the doublets.

The mirrors can be characterized by their spectral collection efficiency η, defined as the ratio of the reflected spectral radiant power to that emitted by the plasma over the full 4π steradian emission range, at wavelength 13.5 nm. The efficiency is determined by the collection and output intensity distributions,

$$\eta = \frac{\int I' \, d\Omega'}{\int I \, d\Omega} \tag{5}$$

where the integrands are defined as in Eq. (3). The FIG. 6A system would be useful for an isotropic emitter characterized by a constant (direction-independent) source intensity I, for which case Eq. (5) simplifies to

$$\eta = \frac{\int R \, d\Omega}{4\pi} \quad \text{(for constant } I\text{)} \tag{6}$$

The mirror reflectance R is a function of ray direction. For ray directions intercepting the mirror doublets (**6.2**) R is the compound two-surface reflectance, averaged over TE and TM polarizations at wavelength 13.5 nm.

Based on the above efficiency metric (Eq. (6)), the calculated collection efficiency of the FIG. 6A system is 51.9% compared to 27.8% for the FIG. 2 mirror. The realistically achievable efficiency would be somewhat lower in both cases because neither value takes into account the laser transmission aperture **1.6** (FIG. 1), and the mirrors **6.2** would require additional openings, e.g. for passing the tin droplets.

Mirror **6.1** in FIG. 6A has higher ellipticity than the mirror **1.4** in FIG. 2. The ratio of the axial plasma-to-mirror distance A to the plasma-to-IF distance B is 0.13 for FIG. 2 and 0.070 in FIG. 6A. Thus, in FIG. 6A either the plasma would need to be much closer to the mirror (smaller A) or the IF would need to be much further from the plasma (larger B). Also, the highly nonuniform output intensity from mirror **6.1** (central peak of curve **7.1** in FIG. 7) is a consequence of the mirror's high ellipticity. The FIG. 6A design could be modified to avoid these drawbacks by keeping A and B the same as FIG. 2 ($A/B = 0.13$), but the range of output angles would need to be increased. The maximum output angle θ' is 11.5º in both FIG. 2 and FIG. 6A. FIG. 8 illustrates an alternative version of the FIG. 6A configuration in which the A/B ratio matches FIG. 2, but the maximum θ' angle is increased to 22.0º. The intensity ratio I'/I versus θ' for this configuration is illustrated in FIG. 9 as curve **9.1**, which is identical to curve **5.2** in FIG. 5 up to θ'=11.5º. The calculated collection efficiency (Eq. (6)) is 52.3%, slightly higher than the FIG. 6A version. But the center-to-edge intensity ratio is 5.8, higher than either of FIG'S. 2 or 6A, because of the large ellipsoid collection angle.

FIG. 10 tabulates summary design data for the collector systems of FIG'S. 2, 6A, and 8. For quantities that are angle-dependent, i.e. functions of θ, the range limits of each quantity corresponding to the θ limits are tabulated. (Separate θ limits are specified for each mirror.) For the doublets, the α and α' angles are the incidence angles on the first and second doublet elements (e.g. on respective elements **6.2.1.1** and **6.2.1.2** of doublet **6.2.1**, FIG. 6C).

The large intensity variation exhibited in FIG. 10 (I'/I column) can be mitigated by using a doublet with a high-angle element, as illustrated in FIG. 11. The collector comprises an ellipsoidal mirror **11.1** similar to element **6.1** in FIG. 6A, a doublet **11.2** comprising low-angle mirror **11.2.1** and high-angle mirror **11.2.2** (similar to the '695 disclosure), and a group **11.3** of doublets comprising low-angle mirrors similar to doublets **6.2** in FIG. 6A. Doublet **11.2** reflects radiation along a path illustrated by ray **11.4**. The low-angle/high-angle combination in doublet **11.2** is more effective at collecting radiation in the angle range between ellipsoid **11.1** and doublet group **11.3**. The center-to-edge output intensity ratio for this design is 3.1, and the collection efficiency is 52.6%.

The A/B ratio in FIG. 11 is 0.082, which is optimized for high efficiency. FIG'S. 12 and 13 illustrate variant designs in which the A/B ratio is constrained to be 0.13, the same as FIG. 2 to maintain the same mirror-to-plasma separation without increasing the overall system length. The output intensity uniformity is also improved relative to FIG. 11. The FIG. 12 system is similar to the '695 disclosure and comprises only the ellipsoid **11.1** and the doublet **11.2** comprising low-angle and high-angle elements **11.2.1** and **11.2.2**. The additional doublets **11.3** are not used. The center-to-edge output intensity ratio for this design is 1.5, and the collection efficiency is 38.5%. The FIG. 13 configuration is similar to FIG. 12 except that there is a ray crossing between elements **11.2.1** and **11.2.2** (e.g., as illustrated by rays **13.1** and **13.2**).

The intensity ratio is 1.2 and the collection efficiency is 45.5%, both significantly better than FIG. 12.

FIG. 14 shows output intensity plots **14.1**-**14.3** corresponding to FIG'S. 11-13, respectively. (The central portions of plots **14.2** and **14.3** are identical to plot **5.2** in FIG. 5 because of the matched A/B ratios.) FIG. 15 tabulates summary design data for the collector systems of FIG'S. 11-13. The doublets in group **11.3** are labeled **11.3.1** … **11.3.6** in the table. The efficiency data (η column in FIG. 15) is somewhat over-optimistic because it does not take into account mirror openings to pass the laser beam and tin droplets. Also, in FIG. 11 mirror **11.2.2** would need to be supported by struts that cross the beam path from doublet group **11.3**.

Plasma irradiation

The efficiency metric defined in Eq. (6) is premised on uniform source intensity, which is not a realistic assumption for existing LPP systems. With a front-irradiated plasma (FIG. 1) most of the EUV is emitted into the laser-facing hemisphere and a greatly extended θ collection range would provide little benefit. However, the extended collection range would be useful if the plasma is irradiated with multiple laser beams. Multibeam systems can significantly improve EUV conversion efficiency [6-9], but the EUV emission is less directionally confined and is not efficiently collected by conventional collection mirrors.

Wide-angle collectors such as those illustrated in FIG'S. 6A, 8, 11, 12, and 13 could be used to more effectively collect plasma emissions in multibeam systems. The laser beams can be directed toward the plasma through aperture openings in the collection mirrors. Highly focused laser beams would efficiently vaporize and ionize comparatively small plasma targets, but the laser spot size could only be reduced by increasing the beam's numerical aperture (convergence angle), which would require larger openings in the collection optics. This limitation can be overcome by using the collection mirrors themselves as wide-angle laser focusing elements. With this approach, the nearly isotropic target irradiance could make it possible to reduce the focused laser spot size by an order of magnitude relative to conventional LPP systems. The collection mirrors can focus both the pre-pulse and main-pulse lasers, although it is possible that the pre-pulse might not be needed with the smaller focus spot.

The collection mirrors can use diffraction gratings to merge the laser and EUV light paths. The gratings can have a blazed form of the type disclosed in U.S. Patent 9,612,370, hereafter '370 [10]. (See FIG'S. 4C, 5, 6, and 7 in '370.) The grating in '370 performs a spectral filtering function, as illustrated in FIG. 16 herein. A laser beam **1.1** irradiates a plasma **1.2**, which emits radiation comprising both short-wave EUV and long-wave out-of-band radiation. The collection mirror **16.1** comprises a blazed diffraction grating, which diffracts EUV radiation into a beam converging toward the IF **1.5**, while long-wave radiation is mostly undiffracted and concentrated in the zero diffraction order, which converges to a ring focus **16.2** surrounding the IF. The wavelength separation is illustrated in FIG. 16 by a plasma-emitted ray **16.3**, which the diffractive mirror separates into EUV ray **16.4** directed toward the IF **1.5** and a long-wavelength ray **16.5** directed toward the ring focus **16.2**. The grating and ring focus have rotational symmetry around axis **2.1**.

Wide-angle collector designs such as those illustrated in FIG'S. 6A, 8, 11, 12, or 13 can be modified to provide spectral filtering as disclosed in '370. The modified central element **6.1** or **11.1** would not be exactly ellipsoidal; it would have a shape determined to direct undiffracted radiation onto the ring focus and would have a grating to diffract 13.5-nm EUV toward the IF as illustrated in FIG. 16. The doublets would be similarly modified, with a diffraction grating formed on at least one of each doublet's two mirrors.

According to '370 the grating operates in essence as a wavelength-selective beam splitter. But it can also operate as a beam combiner, which merges laser radiation into the EUV optical path as illustrated in FIG. 17. [11] (This illustration is based on the FIG. 12 configuration, but any other collection mirror design could be similarly adapted for laser focusing.) A laser beam **1.1** is directed and focused by two beam-forming mirrors **17.1** and **17.2** into a ring focus **17.3** proximate the IF **1.5**. The focused beam is reflected toward collection mirrors **17.4**, **17.5.1**, and **17.5.2** by means of a fold mirror **17.6**, which has a central clear aperture **17.7** ("IF aperture") for passing EUV radiation. (The reflected ring focus surrounds the IF aperture.) The collection mirrors focus the laser radiation onto the plasma target **1.2**, which is ionized and emits EUV radiation. A grating is formed on each of the collection mirrors **17.4** and **17.5.1** to merge the laser beam into the EUV optical path. The grating's period and depth are too small to significantly affect the laser radiation, but the grating efficiently diffracts EUV radiation, separating it from the laser optical path and directing it through the IF aperture **17.7** in the manner disclosed in '370.

The wavelength-combining operation is illustrated in FIG. 17 by laser-generated rays **17.8** and **17.9**, which follow different paths to the plasma target. Ray **17.8** is directed onto the ring focus **17.3** and is reflected by fold mirror **17.6** onto mirror **17.4**, which reflects it along ray path **17.10** toward the plasma **1.2**. Plasma-emitted EUV radiation following the same ray path **17.10** in the opposite direction is diffracted by the grating into ray **17.11**, which is separated from the laser ray **17.8** and is directed through the IF aperture **17.7**. (The EUV-focusing function of mirror **17.4** is similar to mirror **11.1** in FIG. 12.)

Ray **17.9** is also directed onto the ring focus and is reflected first by fold mirror **17.6** and then by mirror **17.5.2** onto mirror **17.5.1**, which reflects it along ray path **17.12** toward the plasma **1.2**. Oppositely-directed EUV radiation following the same ray path **17.12** is diffracted by the grating into ray **17.13**, which is separate from the laser ray **17.9** and is reflected by mirror **17.5.2** toward and through IF aperture **17.7**. (The EUV-focusing function of mirrors **17.5.1** and **17.5.2** is similar to doublet elements **11.2.1** and **11.2.2** in FIG. 12.)

The first beam-forming mirror **17.1** in FIG. 17 shapes the laser beam to control the irradiance distribution on the second mirror **17.2**. This irradiance profile determines the focused laser beam's radiant intensity profile at the plasma. The second mirror **17.2** focuses and shapes the beam into the ring focus **17.3**.

Target viewing

The laser optical path can also be used for plasma target tracking and diagnostics. For example, FIG. 18 illustrates a variant of the laser beam-forming optics in which mirror **17.2** has two small sub-apertures **18.1** and **18.2** for transmitting long-wave radiation that is scattered or emitted by the plasma, focused back onto fold mirror **17.6**, and reflected back toward element **17.2**. The aperture-transmitted radiation **18.3** is captured by cameras **18.4** and **18.5** containing imaging optics and position-sensing detectors, which monitor the target position via parallax viewing and provide feedback for targeting control mechanisms such as the tin droplet generator or laser adaptive optics. A separate viewing wavelength could also be projected through the same mirror system for monitoring the tin droplets before they are irradiated by the main laser pulse.

Multi-laser, multi-focus systems

The laser optics can be adapted to accommodate multiple laser beams. For example, FIG. 19 illustrates two laser beams **19.1** and **19.2** being directed to separate sub-apertures on mirror **17.1**, which can be configured to reflect the separate beams onto substantially non-overlapping sub-apertures on mirror **17.2**.

The system can also be designed to separate the EUV radiation into multiple beams transmitting through different intermediate foci. For example, FIG. 20 illustrates a diffractive collection mirror **20.1**, which receives laser radiation from a ring-focus laser beam that is reflected into the plasma chamber via annular fold mirror **20.2**, and focuses the beam onto plasma **1.2**. Plasma-emitted EUV radiation that intercepts mirror **20.1** is diffractively separated from the laser beam path and focused through an IF aperture **20.3** in mirror **20.2**. Six similar mirror assemblies are arrayed around the plasma to provide wide-angle plasma irradiation and collection. The collection mirrors have central clear apertures such as aperture **20.4** in mirror **20.5** to pass the laser and EUV beams. The system could use multiple lasers, or a single laser beam could be split and partitioned between the different mirrors. This type of system might be useful for EUV metrology systems, which do not need high power but require a compact EUV beam that can be very sharply focused.

Appendix A: Mirror coating design

The mirror designs and performance characteristics discussed in this disclosure are based on a Mo/Si mirror coating design, which is described below. This coating specification is only used for illustrative purposes. Practical coatings might differ significantly from this specification, and the mirror designs might need to be reoptimized and recharacterized based on a more realistic coating design. Also, the coating design would be completely different for design wavelengths other than 13.5 nm, although the illustrated mirror designs are qualitatively applicable to other wavelengths.

The mirror coating is illustrated schematically in FIG. 21. The coating is a multilayer structure **21.1** formed on a Ni (nickel) substrate. There are 50 identical layer periods **21.2**, one of which is shown as **21.3**. Each period includes a Si (silicon) base layer and Mo (molybdenum) top layer, with thin B_4C (boron carbide) diffusion-barrier layers on top of each Si and Mo layer. A capping structure **21.4** including Si, B_4C, and Ru (ruthenium) layers is formed on top of the periodic stack.

The sidebar in FIG. 21 tabulates the assumed complex refractive indices (n) for the optical materials, which are obtained from CXRO [12] using the default material densities. The densities are indicated in FIG. 13. All refractive indices are at wavelength 13.5 nm.

The layer thicknesses are graded to accommodate the variation in incidence angle α across the mirror surfaces. All layers of the same material type (e.g. all Si layers) have the same thickness, which is a function of α. The thicknesses *tSi*, *tMo*, *tRu*, and *tB4C* for the Si, Mo, Ru, and B_4C layers, respectively, have the functional form plotted in FIG. 22 and described by the equations below the plot.

The mirrors' reflectance properties, based on the above specification, are illustrated in FIG. 3. Although the model assumes 50 layer periods, many fewer periods can be used for large incidence angles. For example, for high-angle mirrors ($\alpha > 42.7^\circ$), 25 or fewer layers could be used with little impact on reflectance. For incidence angles above 77º the mirror becomes essentially equivalent to a bare Ru substrate. (The equations in FIG. 22 are only applicable for $\alpha < 77^\circ$.)

Appendix B: Mirror geometry design

The mirror designs illustrated in FIG'S. 6A, 8, 11, 12, and 13 are based on four generic shapes, an ellipsoid and three doublet types, which are described below. The mirror design geometries are illustrated in FIG'S. 23-26. (The ellipsoid, FIG. 23, is conventional, and the design geometry in FIG. 25 is similar to the '695 disclosure.) The following geometry specifications are only for conventional mirrors without the grating as specified in '370. Diffractive collection mirrors such as element **16.1** in FIG. 16 and elements **17.4**, **17.5.1**, and **17.5.2** in FIG. 17 would have a substrate geometry similar to but not exactly identical to the following description.

The ellipsoid geometry (element **1.4** in FIG'S. 1, 2, and 4, element **6.1** in FIG. 6A, element **11.1** in FIG'S. 11, 12, and 13) is illustrated in FIG. 23. $\vec{\mathbf{P}}$, $\vec{\mathbf{P}}'$, and $\vec{\mathbf{X}}$ are Cartesian coordinate vectors. $\vec{\mathbf{P}}$ is the center point of plasma **1.2** in FIG'S. 1, 2, and 4, $\vec{\mathbf{P}}'$ is the intermediate focal point **1.5**, and $\vec{\mathbf{X}}$ is a representative point on the ellipsoid. ($B = |\vec{\mathbf{P}}' - \vec{\mathbf{P}}|$.) θ and θ' are the axial angles of $\vec{\mathbf{X}}$ at points $\vec{\mathbf{P}}$ and $\vec{\mathbf{P}}'$ respectively.

The Law of Sines is applied to the FIG. 23 geometry to obtain the following relations,

$$\frac{|\vec{\mathbf{X}} - \vec{\mathbf{P}}'|}{\sin\theta} = \frac{|\vec{\mathbf{X}} - \vec{\mathbf{P}}|}{\sin\theta'} = \frac{B}{\sin[\theta - \theta']} \tag{7}$$

(Square braces "[…]" delimit function arguments in Eq. (7) and elsewhere in this disclosure.) The ratio of the differential angles $d\theta$ and $d\theta'$ in FIG. 23 is

$$\frac{d\theta'}{d\theta} = \frac{|\mathbf{X}-\mathbf{P}|}{|\mathbf{X}-\mathbf{P}'|} = \frac{\sin\theta'}{\sin\theta} \tag{8}$$

Thus, the differential solid angle ratio $d\Omega / d\Omega'$ in Eq. (4) is

$$\frac{d\Omega}{d\Omega'} = \frac{\sin\theta\, d\theta}{\sin\theta'\, d\theta'} = \frac{\sin^2\theta}{\sin^2\theta'} \tag{9}$$

The ellipsoid shape is defined by the equation

$$|\vec{\mathbf{X}}-\vec{\mathbf{P}}| + |\vec{\mathbf{X}}-\vec{\mathbf{P}}'| = 2A + B \tag{10}$$

Eq. (7) is used to eliminate the vector terms in Eq. (10), and K is defined as

$$K = \frac{2A}{B} + 1 = \frac{\sin\theta + \sin\theta'}{\sin[\theta-\theta']} \tag{11}$$

This relation can be solved for either θ or θ',

$$\sin\theta' = \frac{(K^2-1)\sin\theta}{1+K^2+2K\cos\theta}, \quad \sin\theta = \frac{(K^2-1)\sin\theta'}{1+K^2-2K\cos\theta'} \tag{12}$$

With θ and θ' both known, the vector $\vec{\mathbf{X}}$ position can be determined by triangulation. If the incidence angle α is specified, the substitution $\theta = \theta' + 2\alpha$ (Eq. (1)) can be made in Eq. (11) and the result can be solved for θ',

$$\sin\theta' = \tfrac{1}{2}\left(K\sin[2\alpha] - \sqrt{(1-\cos[2\alpha])\,(2-K^2\,(1-\cos[2\alpha]))}\right) \tag{13}$$

FIG. 24 shows the construction geometry for doublets **6.2** in FIG. 6A and **11.3** in FIG. 11. FIG. 25 represents doublet elements **11.2.1** and **11.2.2** in FIG'S. 11 and 12, and FIG. 26 represents elements **11.2.1** and **11.2.2** in FIG. 13. Each figure depicts an optical ray originating from the plasma center point $\vec{\mathbf{P}}$ with axial angle θ, reflecting from the doublet's first mirror at point $\vec{\mathbf{X}}$ and from the second mirror at point $\vec{\mathbf{X}}'$, and intercepting IF point $\vec{\mathbf{P}}'$ with axial angle θ'. (θ and θ' are positive, and $d\theta'/d\theta$ is negative in FIG'S. 24 and 26, and positive in FIG. 25.) Directional unit vectors $\hat{\boldsymbol{u}}$, $\hat{\boldsymbol{u}}'$, and $\hat{\boldsymbol{u}}''$ are defined for the three ray segments,

$$\hat{\boldsymbol{u}} = \frac{\vec{\mathbf{X}}-\vec{\mathbf{P}}}{|\vec{\mathbf{X}}-\vec{\mathbf{P}}|}, \quad \hat{\boldsymbol{u}}' = \frac{\vec{\mathbf{X}}'-\vec{\mathbf{X}}}{|\vec{\mathbf{X}}'-\vec{\mathbf{X}}|}, \quad \hat{\boldsymbol{u}}'' = \frac{\vec{\mathbf{P}}'-\vec{\mathbf{X}}'}{|\vec{\mathbf{P}}'-\vec{\mathbf{X}}'|} \tag{14}$$

The surface-normal unit vectors $\hat{\boldsymbol{s}}$ at $\vec{\mathbf{X}}$ and $\hat{\boldsymbol{s}}'$ at $\vec{\mathbf{X}}'$ are defined as

$$\hat{\boldsymbol{s}} = \frac{\hat{\boldsymbol{u}}'-\hat{\boldsymbol{u}}}{|\hat{\boldsymbol{u}}'-\hat{\boldsymbol{u}}|}, \quad \hat{\boldsymbol{s}}' = \frac{\hat{\boldsymbol{u}}''-\hat{\boldsymbol{u}}'}{|\hat{\boldsymbol{u}}''-\hat{\boldsymbol{u}}'|} \tag{15}$$

A surface-tangential unit vector $\hat{\boldsymbol{t}}$ at $\vec{\mathbf{X}}$ is defined by rotating $\hat{\boldsymbol{s}}$ clockwise or counterclockwise by 90º, the direction being chosen so that $\hat{\boldsymbol{t}}$ is in the same direction as $d\vec{\mathbf{X}}/d\theta$. Similarly,

surface-tangential unit vector $\hat{\boldsymbol{t}}'$ at $\vec{\mathbf{X}}'$ is defined by rotating $\hat{\boldsymbol{s}}'$ clockwise or counterclockwise by 90º, with $\hat{\boldsymbol{t}}'$ pointing in the same direction as $d\vec{\mathbf{X}}'/d\theta'$ (not $d\vec{\mathbf{X}}'/d\theta$).

$\vec{\mathbf{X}}$ and $\vec{\mathbf{X}}'$ satisfy the following differential equations,

$$\frac{d\vec{\mathbf{X}}}{d\theta} = \hat{\boldsymbol{t}}\frac{|\vec{\mathbf{X}}-\vec{\mathbf{P}}|}{\cos\alpha}, \quad \frac{d\vec{\mathbf{X}}'}{d\theta'} = \hat{\boldsymbol{t}}'\frac{|\vec{\mathbf{X}}'-\vec{\mathbf{P}}'|}{\cos\alpha'} \tag{16}$$

where α and α' are the incidence angles at $\vec{\mathbf{X}}$ and $\vec{\mathbf{X}}'$, respectively. The angles are defined by

$$\cos\alpha = \hat{\boldsymbol{s}}\bullet\hat{\boldsymbol{u}}', \quad \cos\alpha' = \hat{\boldsymbol{s}}'\bullet\hat{\boldsymbol{u}}'' \tag{17}$$

The mirror shapes are determined by combining Eq's. (16) are with an additional condition that controls the output radiant intensity. Eq. (4), which applies to an ellipsoid (FIG. 23), can be generalized as follows for the doublet case,

$$\frac{I'}{I} = \pm R\frac{\sin\theta\, d\theta}{\sin\theta'\, d\theta'} \tag{18}$$

where R is the doublet's compound, two-surface reflectance averaged over TE and TM polarizations, and "$\pm$" is the sign of $d\theta'/d\theta$ ("$-$" in FIG'S. 24 and 26, "$+$" in FIG. 25). The reflectance is a function of the incident angles α and α'. The I'/I intensity ratio can be specified as any function of θ. For the illustrated collector designs the ratio is defined to be a constant,

$$\frac{I'}{I} = \pm C \tag{19}$$

where C is a constant and the sign factor is the same as in Eq. (18). Under this condition $d\theta'/d\theta$ is defined by Eq. (18) and Eq's. (16) define $\vec{\mathbf{X}}$ and $\vec{\mathbf{X}}'$ as functions of a single angle variable θ,

$$\frac{d\vec{\mathbf{X}}}{d\theta} = \hat{\boldsymbol{t}}\frac{|\vec{\mathbf{X}}-\vec{\mathbf{P}}|}{\cos\alpha}, \quad \frac{d\vec{\mathbf{X}}'}{d\theta} = \hat{\boldsymbol{t}}'\frac{|\vec{\mathbf{P}}'-\vec{\mathbf{X}}'|}{\cos\alpha'}\frac{d\theta'}{d\theta} \tag{20}$$

where

$$\frac{d\theta'}{d\theta} = \frac{R}{C}\frac{\sin\theta}{\sin\theta'} \tag{21}$$

Eq. (20) can be numerically solved (e.g. with MATLAB's ode45 function), given initial conditions for $\vec{\mathbf{X}}$ and $\vec{\mathbf{X}}'$.

The illustrated collector designs are configured to maintain continuity of the radiant output intensity across mirror boundaries. The intensity ratio I'/I at the edge of the ellipsoid in FIG'S. 6A, 11, 12, and 13 is given by Eq. (4) (with substitution from Eq. (9)), and this value is used to set the C constant (Eq. (19)), which is the same (except for possible sign differences) for all doublets.

For the FIG. 24 configuration, boundary conditions for Eq's. (20) are determined so that the collected beam from point $\vec{\mathbf{P}}$ and the output beam directed toward $\vec{\mathbf{P}}'$ both efficiently fill the mirror apertures, as illustrated in FIG. 27. The θ integration limits are θ_1 and θ_2:

$$\theta_1 \le \theta \le \theta_2 \tag{22}$$

The corresponding limits on θ' are θ'_2 and θ'_1,

$$\theta'_1 \le \theta' \le \theta'_2, \quad \theta'_1 = \theta'[\theta_2], \quad \theta'_2 = \theta'[\theta_1] \tag{23}$$

θ_1, θ_2, and θ'_1 are specified and θ'_2 is determined to satisfy the aperture-filling condition. (In FIG. 6B, for example, the angle limits θ_1 and θ'_1 for doublet **6.2.1** are defined by the θ and θ' limits of ellipsoid **6.1**, and the doublet's θ_2 limit determines its aperture size. The angle limits θ_1 and θ'_1 for doublet **6.2.2** are defined by the θ_2 and θ'_2 limits of doublet **6.2.1**, and similarly for doublets **6.2.3**, etc.)

The first mirror is defined by points $\vec{\mathbf{X}}[\theta]$ and the second mirror is defined by points $\vec{\mathbf{X}}'[\theta]$, both parameterized as functions of θ, $\theta_1 \le \theta \le \theta_2$. The ray from plasma point $\vec{\mathbf{P}}$ to the first mirror's point $\vec{\mathbf{X}}[\theta_1]$ intercepts the second mirror's aperture point $\vec{\mathbf{X}}'[\theta_2]$. Thus, point $\vec{\mathbf{X}}'[\theta_2]$ has axial angle θ_1 at $\vec{\mathbf{P}}$ and axial angle θ'_1 at $\vec{\mathbf{P}}'$, from which the point's location can be determined by triangulation. Similarly, the ray from the second mirror's point $\vec{\mathbf{X}}'[\theta_1]$ to $\vec{\mathbf{P}}'$ intercepts the first mirror's aperture point $\vec{\mathbf{X}}[\theta_2]$, which thus has axial angle θ_2 at $\vec{\mathbf{P}}$ and axial angle θ'_2 at $\vec{\mathbf{P}}'$. Given θ_2 and an initial estimate of θ'_2, the location of $\vec{\mathbf{X}}[\theta_2]$ is also determined by triangulation and the full mirror geometry is determined by integrating Eq's. (20) from $\theta = \theta_2$ to $\theta = \theta_1$. The resultant point $\vec{\mathbf{X}}'[\theta_1]$ on the second mirror will not necessarily have axial angle θ'_2 at $\vec{\mathbf{P}}'$, so the θ'_2 estimate will need to be iteratively refined (e.g., using the secant method) until the angle constraint is satisfied.

If the mirror reflectance R in Eq. (21) were constant, then the equation could be integrated directly to obtain θ'_2 directly, without resorting to an iterative numerical solution:

$$R = \text{constant} \quad \rightarrow \quad d\cos\theta' = \frac{R}{C} d\cos\theta, \quad \cos\theta'_1 - \cos\theta'_2 = \frac{R}{C}(\cos\theta_1 - \cos\theta_2) \tag{24}$$

More generally, a constant approximation to R can be used in Eq. (24) to determine an initial θ'_2 estimate for the above-described iterative refinement process.

Addendum 1

The mirror geometry design outlined in Appendix B does not apply to diffractive mirrors. Following is a generalized design procedure, which includes the diffraction grating.

The ellipsoidal focusing mirror illustrated in FIG. 23 can be modified to include a diffraction grating. The modified mirror will not be exactly ellipsoidal and will not be defined by Eq's. (8)-(13), but its shape can be determined by solving a differential equation. The geometry underlying the equation is illustrated in FIG. 28.

An optical ray **28.1** originating from plasma point $\vec{\mathbf{P}}$ at axial angle θ intercepts the mirror **28.2** at point $\vec{\mathbf{X}}$ and reflects into two rays: a diffracted ray **28.3**, which intercepts intermediate focal point $\vec{\mathbf{P}}'$, and an undiffracted ray **28.4**, which is directed away from the intermediate focus. Unit vectors along these three ray directions are indicated as $\hat{\boldsymbol{u}}$, $\hat{\boldsymbol{u}}'^{[1]}$, and $\hat{\boldsymbol{u}}'^{[0]}$, and the diffractive deviation angle between vectors $\hat{\boldsymbol{u}}'^{[0]}$ and $\hat{\boldsymbol{u}}'^{[1]}$ is δ. $\hat{\boldsymbol{u}}$ and $\hat{\boldsymbol{u}}'^{[1]}$ are defined as

$$\hat{\boldsymbol{u}} = \frac{\vec{\mathbf{X}} - \vec{\mathbf{P}}}{|\vec{\mathbf{X}} - \vec{\mathbf{P}}|}, \quad \hat{\boldsymbol{u}}'^{[1]} = \frac{\vec{\mathbf{P}}' - \vec{\mathbf{X}}}{|\vec{\mathbf{P}}' - \vec{\mathbf{X}}|} \tag{25}$$

$\hat{\boldsymbol{u}}'^{[0]}$ is determined by rotating vector $\hat{\boldsymbol{u}}'^{[1]}$ by angle δ (clockwise in the plane of FIG. 28 if δ is positive, counterclockwise if δ is negative). The zero order is unaffected by the presence of the diffraction grating; its direction is determined by the law of reflection at the grating substrate. Consequently, the substrate normal vector $\hat{\boldsymbol{s}}$ at $\vec{\mathbf{X}}$ is defined by

$$\hat{\boldsymbol{s}} = \frac{\hat{\boldsymbol{u}}'^{[0]} - \hat{\boldsymbol{u}}}{|\hat{\boldsymbol{u}}'^{[0]} - \hat{\boldsymbol{u}}|} \tag{26}$$

The substrate tangent vector $\hat{\boldsymbol{t}}$ at $\vec{\mathbf{X}}$ is defined by rotating $\hat{\boldsymbol{s}}$ counterclockwise in the plane of FIG. 28. With the deviation angle δ defined as a function of $\vec{\mathbf{X}}$ and/or θ, $\vec{\mathbf{X}}$ satisfies the following differential equation,

$$\frac{d\vec{\mathbf{X}}}{d\theta} = \hat{\boldsymbol{t}} \frac{|\vec{\mathbf{X}} - \vec{\mathbf{P}}|}{\cos\alpha^{[0]}} \tag{27}$$

where $\alpha^{[0]}$ is the zero-order incidence angle defined by

$$\cos\alpha^{[0]} = -\hat{\boldsymbol{s}} \bullet \hat{\boldsymbol{u}} = \hat{\boldsymbol{s}} \bullet \hat{\boldsymbol{u}}'^{[0]} \tag{28}$$

For the doublet mirror designs, a similar procedure can be used to accommodate a diffraction grating. For example, if the grating is on the first element the following modifications are made to the equations in Appendix B: In Eq. (14) $\hat{\boldsymbol{u}}'$ is replaced by $\hat{\boldsymbol{u}}'^{[1]}$, the diffracted ray vector:

$$\hat{\boldsymbol{u}} = \frac{\vec{\mathbf{X}} - \vec{\mathbf{P}}}{|\vec{\mathbf{X}} - \vec{\mathbf{P}}|}, \quad \hat{\boldsymbol{u}}'^{[1]} = \frac{\vec{\mathbf{X}}' - \vec{\mathbf{X}}}{|\vec{\mathbf{X}}' - \vec{\mathbf{X}}|}, \quad \hat{\boldsymbol{u}}'' = \frac{\vec{\mathbf{P}}' - \vec{\mathbf{X}}'}{|\vec{\mathbf{P}}' - \vec{\mathbf{X}}'|} \tag{29}$$

($\hat{\boldsymbol{u}}''$ is the reflection of $\hat{\boldsymbol{u}}'^{[1]}$ off the second mirror element.) In Eq. (15) $\hat{\boldsymbol{u}}'^{[0]}$ is used in defining $\hat{\boldsymbol{s}}$, but $\hat{\boldsymbol{u}}'^{[1]}$ is used to define $\hat{\boldsymbol{s}}'$,

$$\hat{\boldsymbol{s}} = \frac{\hat{\boldsymbol{u}}'^{[0]} - \hat{\boldsymbol{u}}}{|\,\hat{\boldsymbol{u}}'^{[0]} - \hat{\boldsymbol{u}}\,|}, \quad \hat{\boldsymbol{s}}' = \frac{\hat{\boldsymbol{u}}'' - \hat{\boldsymbol{u}}'^{[1]}}{|\,\hat{\boldsymbol{u}}'' - \hat{\boldsymbol{u}}'^{[1]}\,|} \tag{30}$$

In Eq's. (16) and (17) α is the zero-order incident angle, $\alpha^{[0]}$,

$$\frac{d\vec{\mathbf{X}}}{d\theta} = \hat{\boldsymbol{t}}\,\frac{|\,\vec{\mathbf{X}} - \vec{\mathbf{P}}\,|}{\cos\alpha^{[0]}}, \quad \frac{d\vec{\mathbf{X}}'}{d\theta'} = \hat{\boldsymbol{t}}'\,\frac{|\,\vec{\mathbf{X}}' - \vec{\mathbf{P}}'\,|}{\cos\alpha'} \tag{31}$$

$$\cos\alpha^{[0]} = -\hat{\boldsymbol{s}}\bullet\hat{\boldsymbol{u}} = \hat{\boldsymbol{s}}\bullet\hat{\boldsymbol{u}}'^{[0]}, \quad \cos\alpha' = -\hat{\boldsymbol{s}}'\bullet\hat{\boldsymbol{u}}'^{[1]} = \hat{\boldsymbol{s}}'\bullet\hat{\boldsymbol{u}}'' \tag{32}$$

A variety of possible collection mirror designs are illustrated in FIG'S. 6.A, 8, 11, 12, and 13. FIG. 29A illustrates another possible configuration, which includes diffraction gratings. The collector comprises a diffractive low-angle mirror **29.1** of the type illustrated in FIG. 28, and two mirror doublets **29.2** and **29.3** similar to that illustrated in FIG. 25 but with diffraction gratings designed according to Eq's. (29)-(32). Doublet **29.2** comprises low-angle element **29.2.1** and high-angle element **29.2.2**, and doublet **29.3** comprises low-angle element **29.3.1** and high-angle element **29.3.2**. Diffraction gratings are formed on elements **29.1**, **29.2.1** and **29.3.1**. (The grating on element **29.1** is shown in cross section as **29.4** in the expanded view of FIG. 29B.) Design and performance data for this configuration are tabulated in FIG. 30, and FIG. 31 shows its output intensity plot **31.1** in comparison the plot **5.2** for the FIG. 2 ellipsoid.

In FIG. 30 α is the incidence angle on elements **29.1**, **29.2.1** and **29.3.1**, and α' is the incidence angle on elements **29.2.2** and **29.3.2**. The α angle is the incidence angle relative the the grating facet surfaces (not the grating substrate), under the assumption that a conformal multilayer grating is used. The efficiency data is estimated under the assumption that the grating's EUV diffraction efficiency is substantially identical to a conventional multilayer mirror operating at the same incidence angle.

In the illustrated design, the deviation angle δ (cf. FIG. 28) for element **29.1** is 5.87 mrad over the full mirror aperture, and the resulting grating period varies from 2.8 micron to 2.9 micron from center to edge. For element **29.2.1**, δ is a linear function of θ varying from -4.69 mrad at the inner radius to -1.23 mrad at the outer radius, and the corresponding period variation is 3.9 micron to 5.7 micron. For element **29.3.1**, δ is also a linear function of θ varying from -3.45 mrad at the inner radius to -2.59 mrad at the outer radius, and the corresponding period variation is 3.2 micron to 13.5 micron. If a conformal multilayer grating is used, the grating depth varies from 6.8 nm at the center of element **29.1** to 8.2 nm at the outer edge of element **29.3.1**.

Addendum 2

Grating Manufacture

A phase-Fresnel EUV reflection grating, such as that depicted schematically in FIG. 29B, can be designed either as a conformal multilayer grating or as a patterned multilayer grating as disclosed in U.S. Patent 9,612,370 (Ref. [10]). Conformal multilayer gratings can be manufactured by the method described below.

As disclosed in '370, a conformal multilayer grating is constructed as a substrate having a phase-Fresnel surface-relief structure, and a multilayer, reflective film stack comprising Mo/Si bilayers deposited conformally on the phase-Fresnel structure. The phase-Fresnel structure can be patterned in the substrate by the method illustrated in FIG'S. 32A-32C. A substrate surface **32.1**, shown in cross-section, is machined and polished to a high degree of smoothness, e.g. less than 0.2-nm roughness. (The surface is generally curved, although it is schematically illustrated as flat in FIG'S. 32A-32C.) A sacrificial layer **32.2** is then deposited on substrate **32.1**. The layer material should have good machinability characteristics and should be capable of being etched by a method such as ion beam etching, wet chemical etching, etc. Furthermore, the substrate material should also be capable of being etched by the same process, but preferably at an etch rate much slower than the sacrificial layer.

A blazed grating structure **32.3** is machined into layer **32.2**, preferably using a diamond turning process with the cutting tool and process conditions optimized to achieve the best possible surface finish on the grating. For example, a diamond tool **32.4** with a straight cutting edge defined by the diamond crystal planes would form smooth grating facets.

The structure is then blanket-etched to transfer the machined grating pattern into the substrate, FIG. 32C. The resulting grating **32.5** can be much shallower than the original machined grating if the substrate etches slower than the sacrificial layer. Any machining marks or irregularities will consequently be scaled down in the final grating, resulting in a smoother and more accurately contoured surface. Conformal multilayer gratings would typically have a substrate pattern depth in the range of 7 to 10 nm, compared to the grating period of over 2 microns, and high-fidelity, shallow gratings of this type can be formed using the sacrificial layer method described above.

A manufacturing process of this type is reported in [13]. (See Figure 11.) In this work the authors formed a mechanically ruled, blazed grating in a gold layer on silicon, which was then transferred into the silicon via ion beam etching. The etch process reduced the blaze angle from 6.6° to 0.62°, and the surface roughness was reduced from 0.56 nm r.m.s. to 0.12 nm r.m.s. The grating was formed using a ruling engine, but the same process could be used with diamond-turned gratings.

The diamond turning operation illustrated in FIG. 32B can be accurately controlled by using an interferometric depth gauge as illustrated schematically in FIG. 33. An optical interferometer **33.1** directs two focused, coherent optical beams **33.2** and **33.3** onto the workpiece, one onto the cut surface and one onto the uncut surface adjacent to the grating step. The beams reflect off the surfaces and are combined in the interferometer to detect their relative optical phase, which provides an accurate measure of the depth of cut for tool control.

The patterned substrate can be blanket-coated with a conformal, multilayer Mo/Si reflectance stack as disclosed in '370. The grating edges will cause slight irregularities in the deposited films in the vicinity of the edges. The irregularities can reduce diffraction efficiency somewhat, particularly if the grating period is fairly short. However, an alternative deposition process could be used to eliminate the irregularities and maximize diffraction efficiency.

In the alternative method, illustrated in FIG. 34, a masked ion-beam deposition process is used in which each Mo/Si bilayer is deposited over limited area covering a whole number of grating periods on the substrate **34.1**. For example, the figure illustrates bilayer **34.2** being deposited by ion beam **34.3** through mask **34.4**, which covers four periods. The substrate is positionally stepped by one period between successive bilayer depositions so that the bilayers form Bragg diffraction planes extending seamlessly across the grating edges.

In a variation of this method, illustrated in FIG. 35, the bilayers are deposited on a unpatterned substrate. Rather than moving the substrate in discrete steps between bilayer depositions, it is moved continuously by one period per bilayer during the deposition process.

References

[1] ANSI/IES RP-16-17, Nomenclature and Definitions for Illuminating Engineering https://www.ies.org/standards/ansi-ies-rp-16/

[2] A. Hassanein, V. Sizyuk, S. S. Harilal, T. Sizyuk, "Analysis, simulation, and experimental studies of YAG and CO2 laser-produced plasma for EUV lithography sources", Proc. SPIE 7636, Extreme Ultraviolet (EUV) Lithography, 76360A (20 March 2010). https://doi.org/10.1117/12.848222

[3] J. Sasian, "Efficient EUV collector designs", U.S. Patent 7,405,871, July 29, 2008.

[4] R. Geyl, et al., "Device for collecting flux of electromagnetic radiation in the extreme ultraviolet", U.S. Patent 8,023,182, September 20, 2011.

[5] M. Endres, "EUV collector", U.S. Patent 9,754,695, September 5, 2017.

[6] A. J. Comley, et al., "Laser Multiplexing", U.S. Patent Application 2007/0272669, November 29, 2007.

[7] Y. Shimada, et al., "Characterization of extreme ultraviolet emission from laser-produced spherical tin plasma generated with multiple laser beams", Appl. Phys. Lett. 86, 051501 (2005). https://doi.org/10.1063/1.1856697

[8] V. Sizyuk, A. Hassanein, and T. Sizyuk, "Three-dimensional simulation of laser-produced plasma for extreme ultraviolet lithography applications", Journal of Applied Physics 100, 103106 (2006). https://doi.org/10.1063/1.2365717

[9] K. Yoshida, et al., "Beyond Extreme Ultra Violet (BEUV) Radiation from Spherically symmetrical High-Z plasmas", 2016 J. Phys.: Conf. Ser. 688 012046. https://doi.org/10.1088/1742-6596/688/1/012046

[10] K. Johnson, “EUV light source with spectral purity filter and power recycling”, U.S. Patent 9,612,370, April 4, 2017.

[11] K. Johnson, “EUV Source Optics with 100% OOB Exclusion”, 2018 EUVL Workshop https://www.euvlitho.com/2018/P14.pdf

[12] CXRO refractive index data:
B.L. Henke, E.M. Gullikson, and J.C. Davis. X-ray interactions: photoabsorption, scattering, transmission, and reflection at E=50-30000 eV, Z=1-92, Atomic Data and Nuclear Data Tables Vol. 54 (no.2), 181-342 (July 1993).
http://henke.lbl.gov/optical_constants/getdb2.html

[13] “Gratings for synchrotron and FEL beamlines: a project for the manufacture of ultra-precise gratings at Helmholtz Zentrum Berlin”, F. Siewert et al., J. Synchrotron Rad. (2018). 25, 91–99.
https://doi.org/10.1107/S1600577517015600
https://journals.iucr.org/s/issues/2018/01/00/xl5026/xl5026.pdf

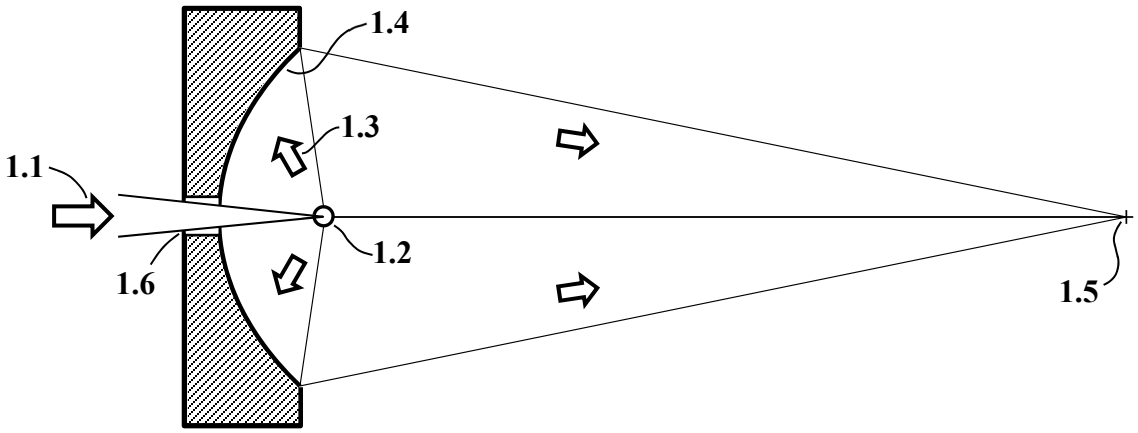

FIG. 1

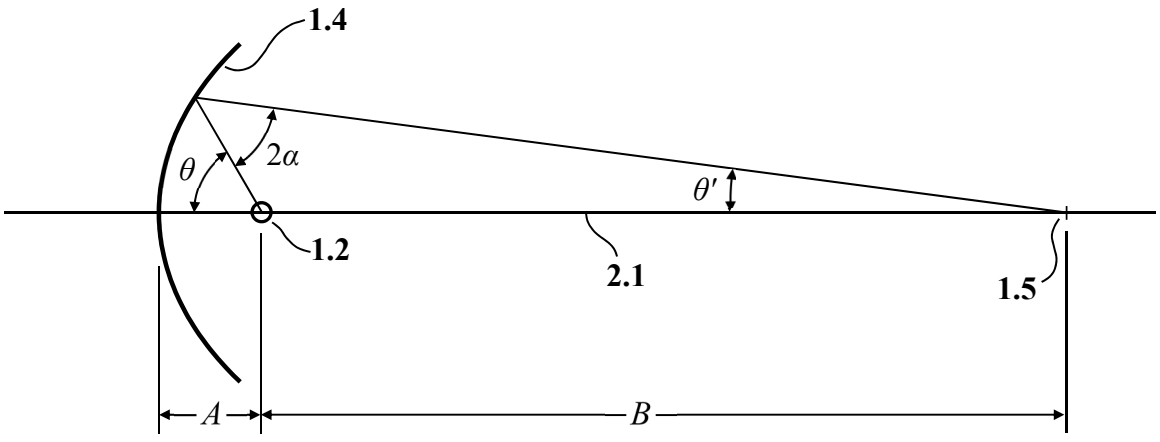

FIG. 2

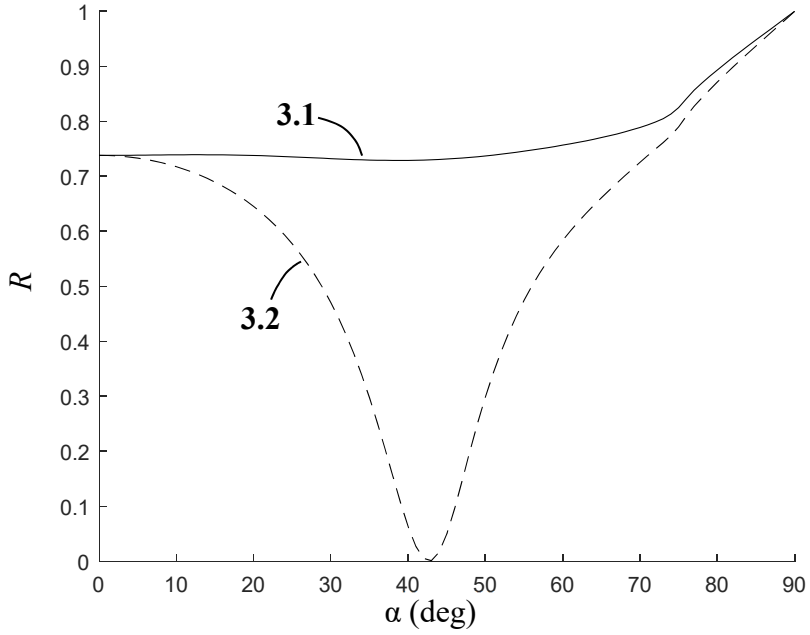
1
0.9
0.8
0.7
0.6
0.5
0.4
0.3
0.2
0.1
0
R
3.1
3.2
0
10
20
30
40
50
60
70
80
90
α (deg)

FIG. 3

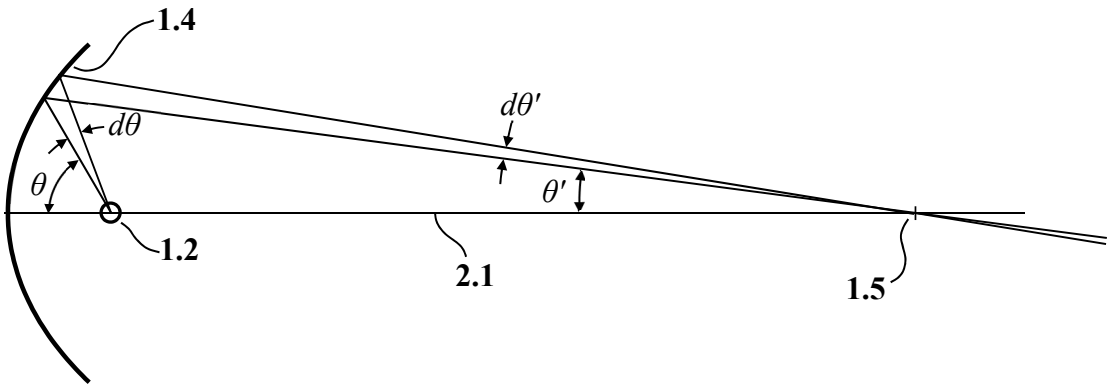
1.4
dθ
dθ′
θ
θ′
1.2
2.1
1.5

FIG. 4

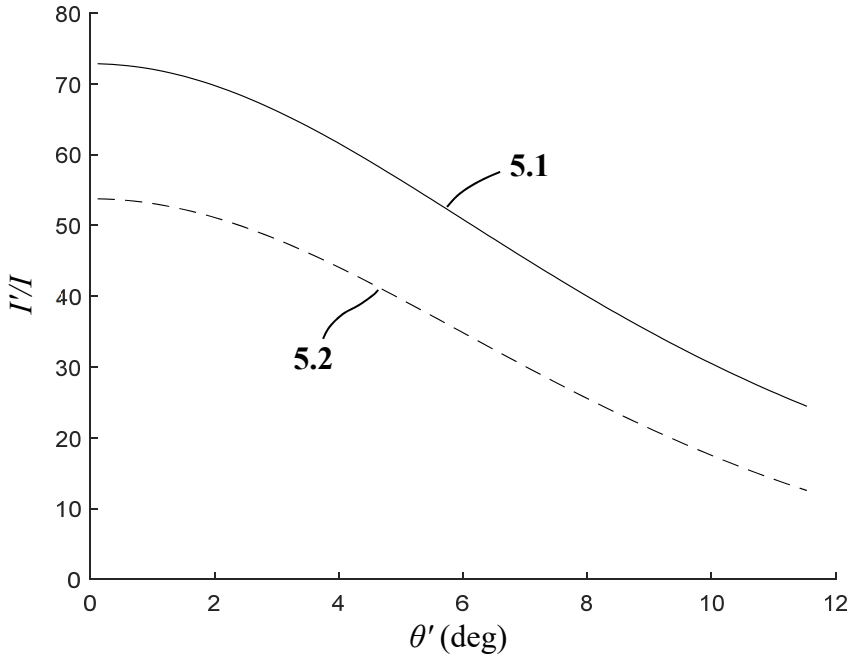
80
70
60
50
40
30
20
10
0
I′/I
0
2
4
6
8
10
12
θ′ (deg)
5.1
5.2

FIG. 5

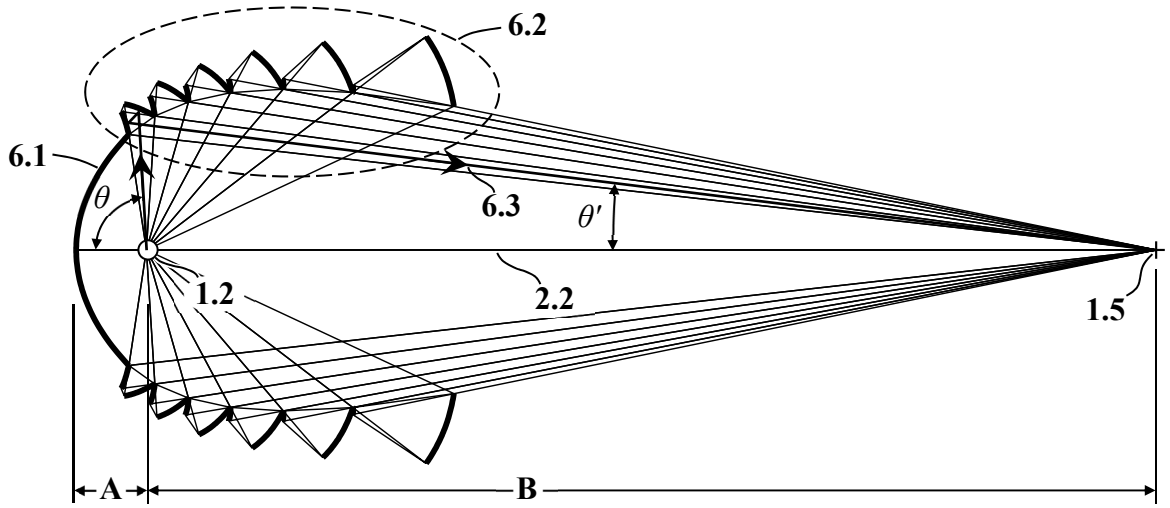
6.2
6.1
θ
6.3
θ′
1.2
2.2
1.5
A
B

FIG. 6A

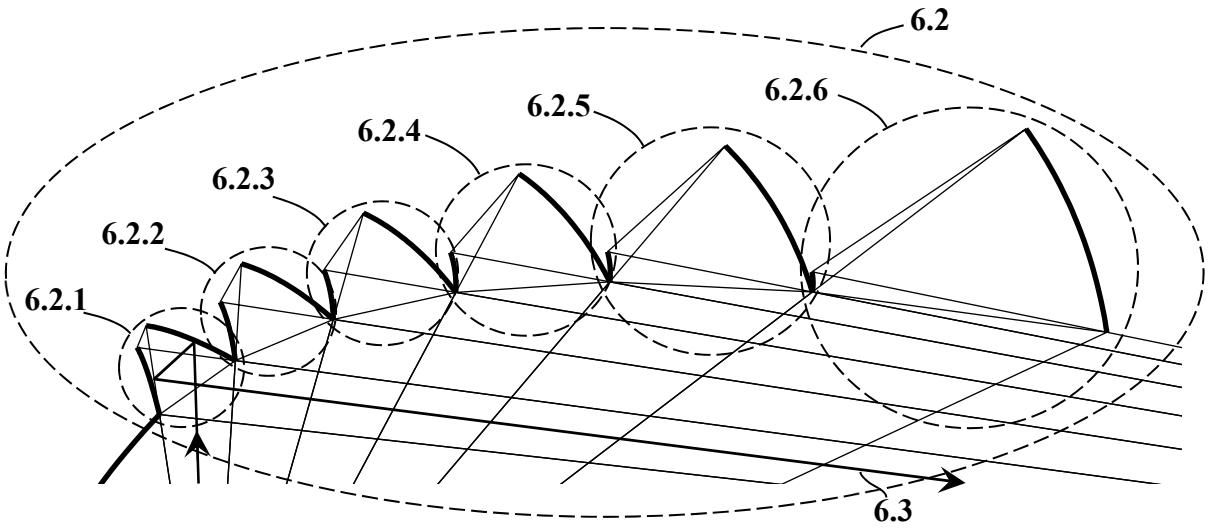

FIG. 6B

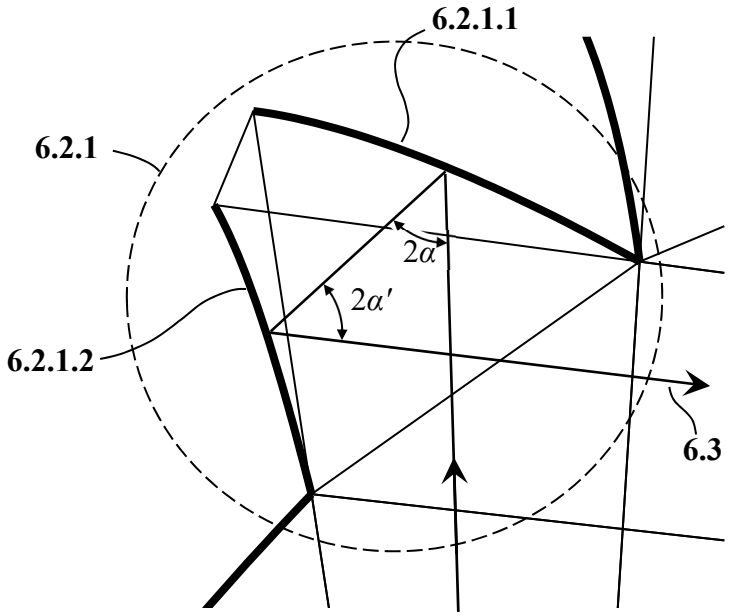

FIG. 6C

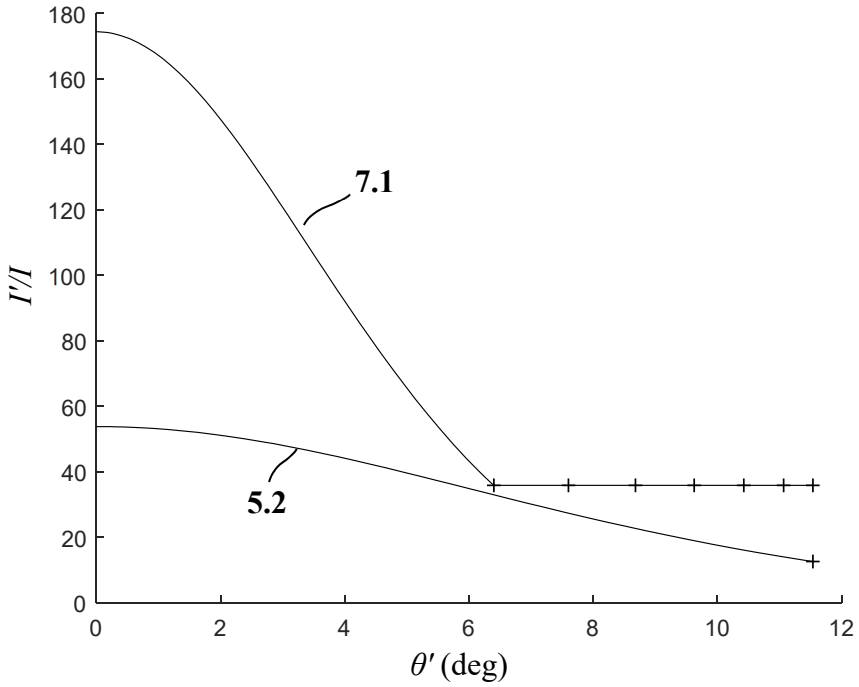

FIG. 7

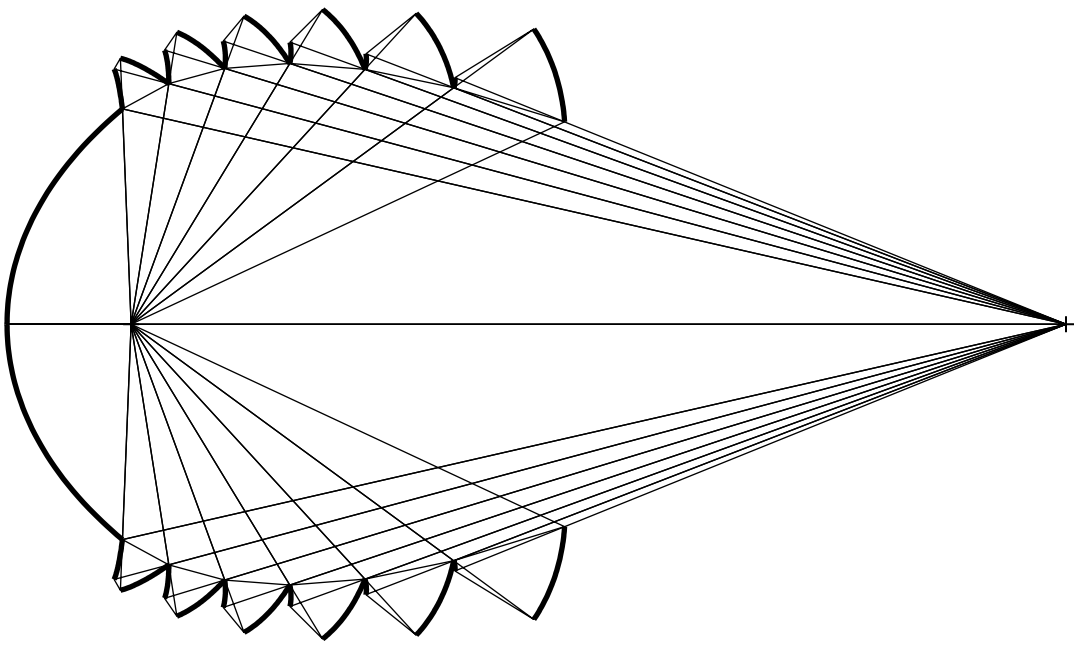

FIG. 8

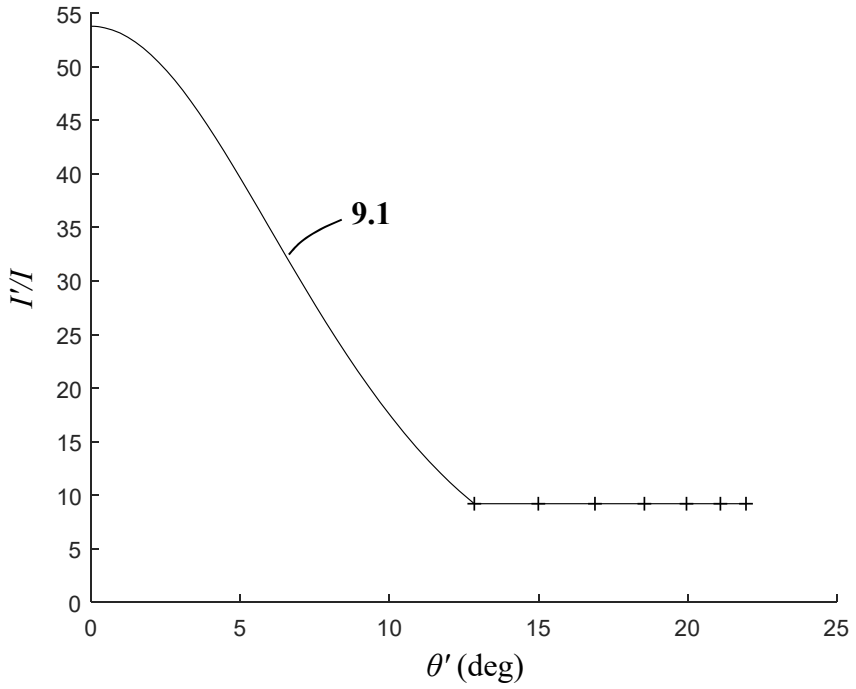

FIG. 9

	mirror	η	I'/I	A/B	θ (deg)	θ' (deg)	α (deg)	α' (deg)
FIG. 2	**1.4**	0.278	53.8…12.6	0.133	0…81.54	0…11.54	0…35.00	
FIG. 6A	**6.1**	0.269	174.4…35.8	0.0696	0…81.34	0…6.40	0…37.47	
	6.2.1	0.0458	35.8		81.34…93.62	7.60…6.40	15.66…25.5	37.47…20.86
	6.2.2	0.0477	35.8		93.62…105.89	8.68…7.60	12.75…25.68	34.78…15.17
	6.2.3	0.0470	35.8		105.89…118.17	9.63…8.68	9.55…24.71	32.32…10.55
	6.2.4	0.0435	35.8		118.17…130.45	10.42…9.63	6.49…22.83	29.64…6.76
	6.2.5	0.0374	35.8		130.45…142.72	11.07…10.42	3.84…20.07	26.47…3.78
	6.2.6	0.0289	35.8		142.72…155.00	11.54…11.07	1.81…16.38	22.60…1.66
	6.1 & **6.2** total	0.519			0…155.00	0…11.54		
FIG. 8	**6.1**	0.304	53.8…9.2	0.133	0…87.71	0…12.85	0…37.43	
	6.2.1	0.0416	9.2		87.71…98.93	14.99…12.85	16.21…26.29	37.43…20.67
	6.2.2	0.0420	9.2		98.92…110.14	16.90…14.99	12.83…27.34	36.16…15.09
	6.2.3	0.0406	9.2		110.14…121.36	18.55…16.90	9.74…27.12	34.47…10.65
	6.2.4	0.0374	9.2		121.36…132.57	19.96…18.55	6.87…25.96	32.43…7.03
	6.2.5	0.0322	9.2		132.57…143.79	21.10…19.96	4.34…23.94	29.92…4.15
	6.2.6	0.0253	9.2		143.79…155.00	21.96…21.10	2.30…21.05	26.79…2.00
	6.1 & **6.2** total	0.523			0…155.00	0…21.96		

FIG. 10

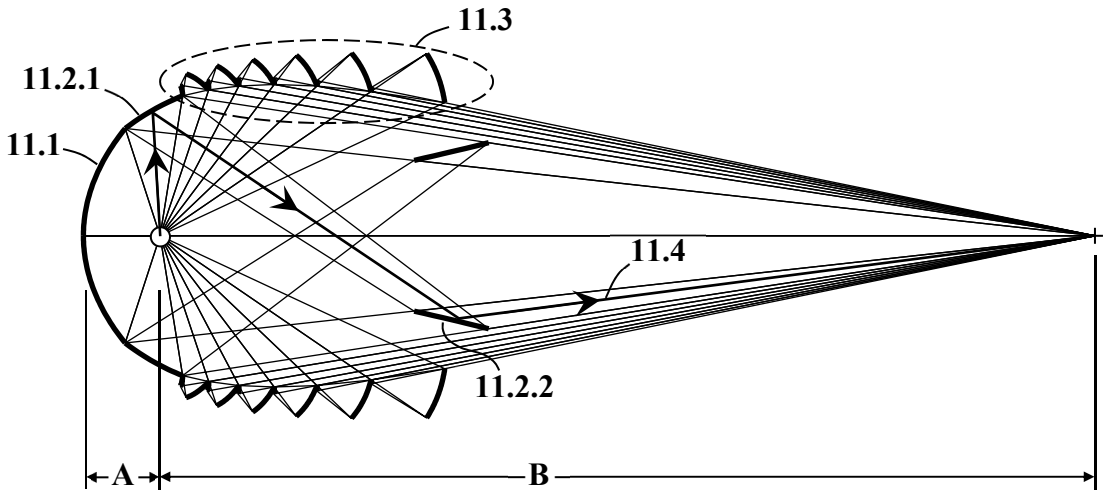

FIG. 11

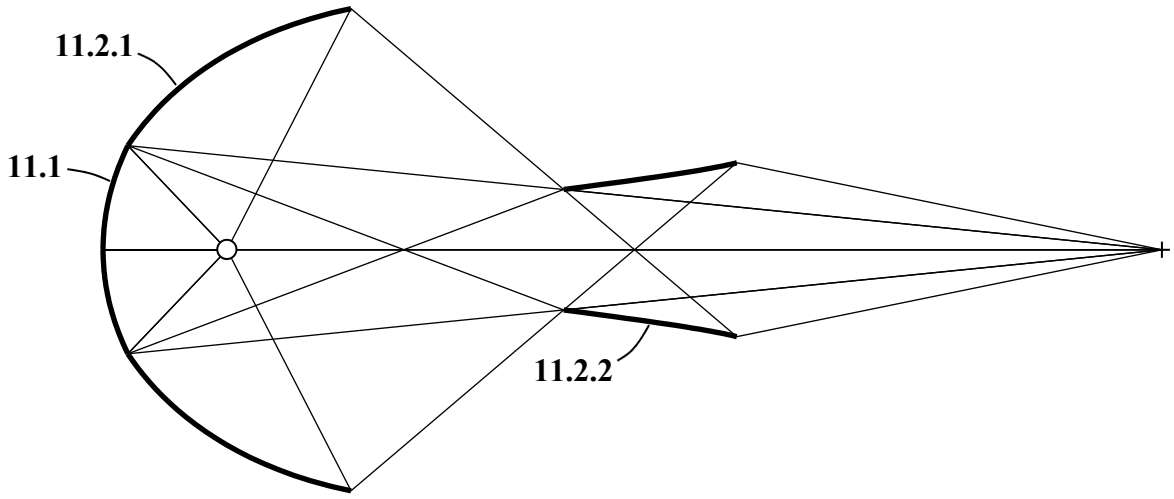

FIG. 12

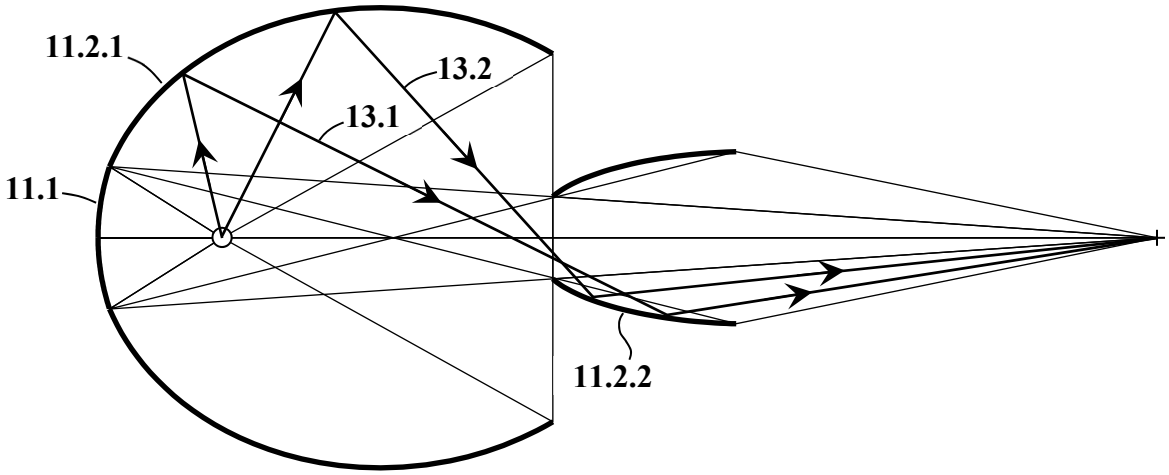
11.2.1
13.2
13.1
11.1
11.2.2

FIG. 13

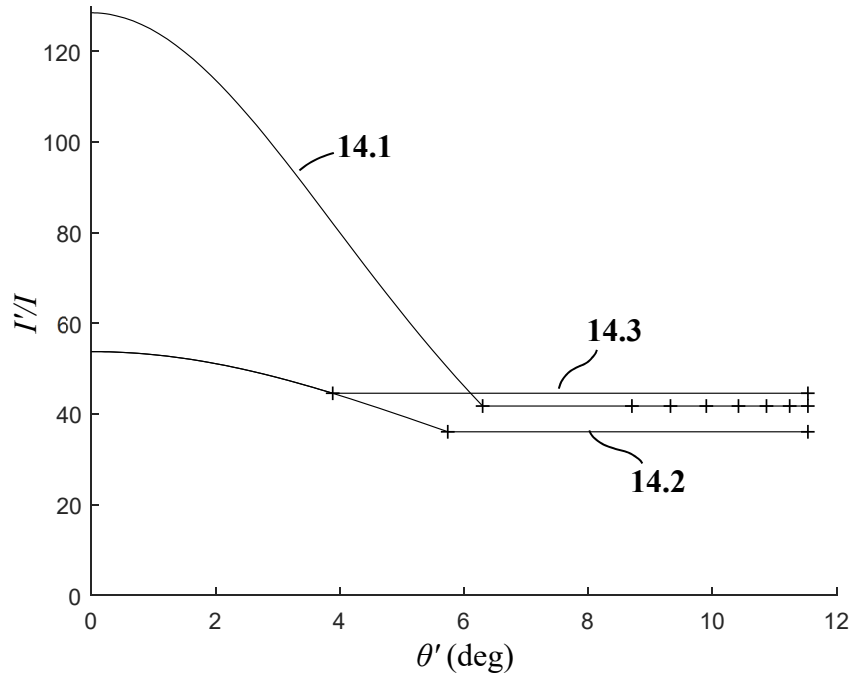
120
100
80
60
40
20
0
I'/I
14.1
14.3
14.2
0
2
4
6
8
10
12
θ′ (deg)

FIG. 14

	mirror	η	I' / I	A / B	θ (deg)	θ' (deg)	α (deg)	α' (deg)
FIG. 11	**11.1**	0.230	128.5…41.8	0.082	0…71.97	0…6.30	0…32.84	
	11.2	0.114	41.8		71.97…99.20	6.30…8.70	19.86…30.98	70.73…67.03
	11.3.1	0.0355	41.8		99.20…108.50	9.3…8.70	9.10…29.41	35.96…10.69
	11.3.2	0.0351	41.8		108.50…117.80	9.90…9.33	7.61…27.39	33.10…8.37
	11.3.3	0.0334	41.8		117.80…127.10	10.42…9.90	5.86…25.24	30.46…6.16
	11.3.4	0.0303	41.8		127.10…136.40	10.87…10.42	4.13…22.82	27.75…4.19
	11.3.5	0.0262	41.8		136.40…145.70	11.25…10.87	2.61…20.04	24.82…2.54
	11.3.6	0.0210	41.8		145.70…155.00	11.54…11.25	1.40…16.82	21.52…1.30
	11.1-3 total	0.526			0…155.00	0…11.54		
FIG. 12	**11.1**	0.111	53.8…36.1	0.133	0…46.32	0…5.74	0…20.29	
	11.2	0.274	36.1		46.32…117.24	5.74…11.54	12.85…38.46	76.82…64.07
	11.1-2 total	0.385			0…117.24	0…11.54		
FIG. 13	**11.1**	0.056	53.8…44.6	0.133	0…32.29	0…3.89	0…14.20	
	11.2	0.399	44.6		32.29…150.94	11.54…3.89	9.11…30.47	77.20…43.06
	11.1-2 total	0.455			0…150.94	0…11.54		

FIG. 15

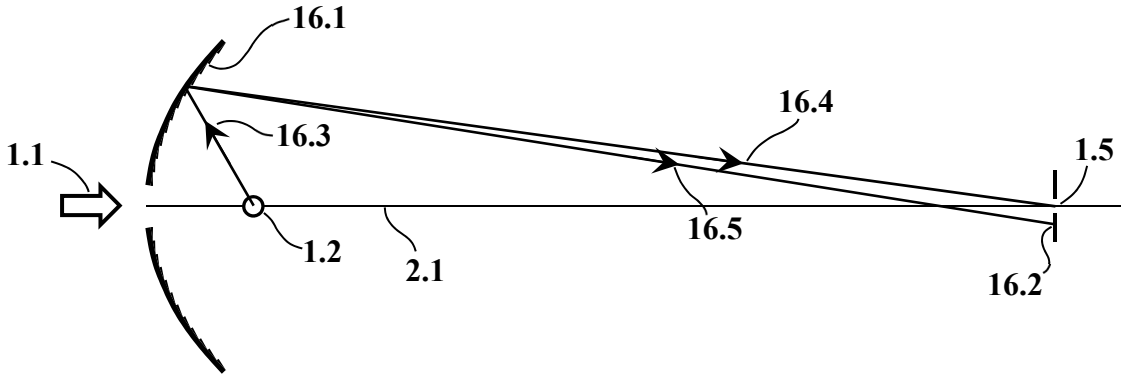

FIG. 16

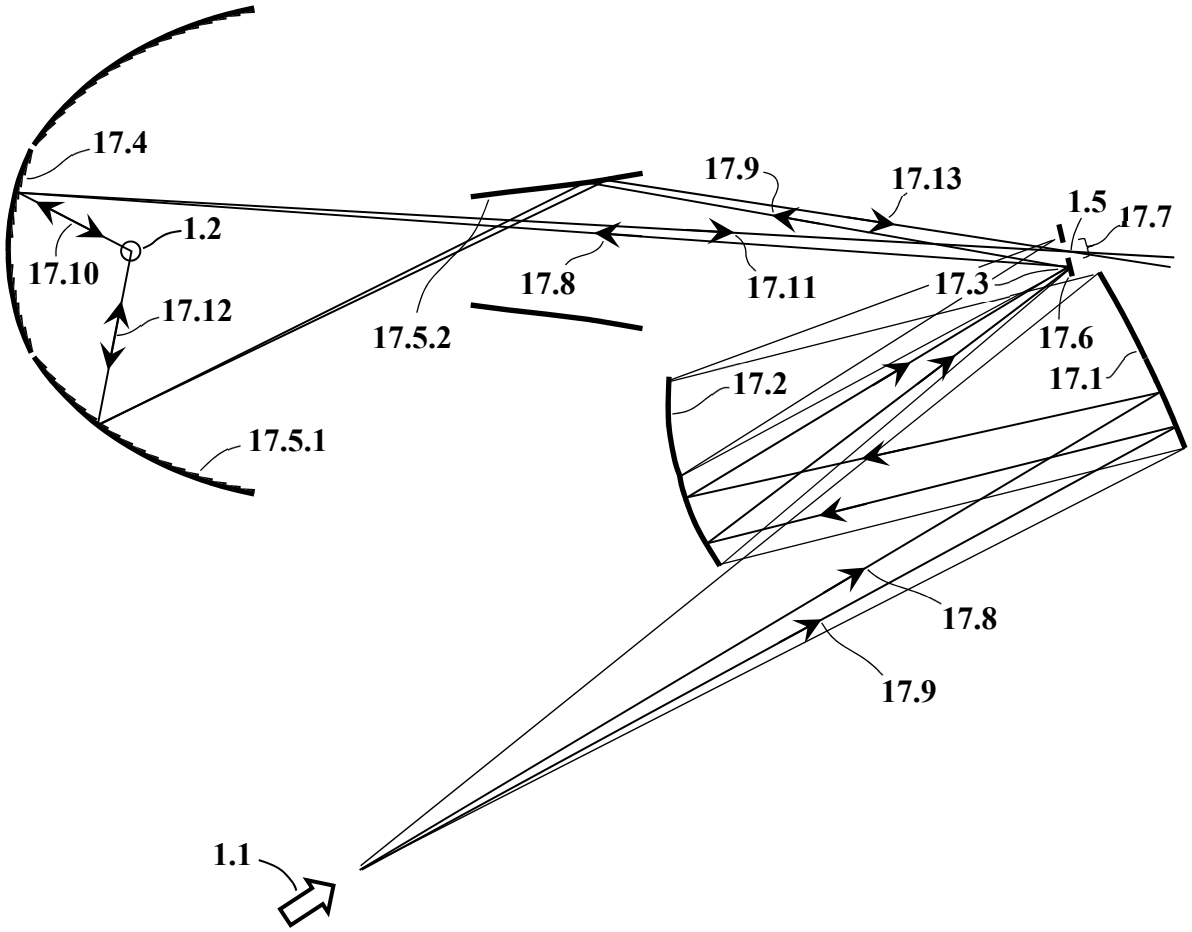
17.4
17.9
17.13
1.5
17.7
1.2
17.10
17.8
17.11
17.3
17.12
17.5.2
17.6
17.2
17.1
17.5.1
17.8
17.9
1.1

FIG. 17

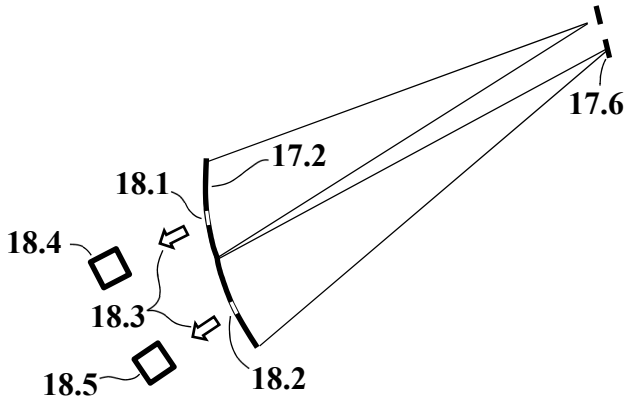
17.6
17.2
18.1
18.4
18.3
18.5
18.2

FIG. 18

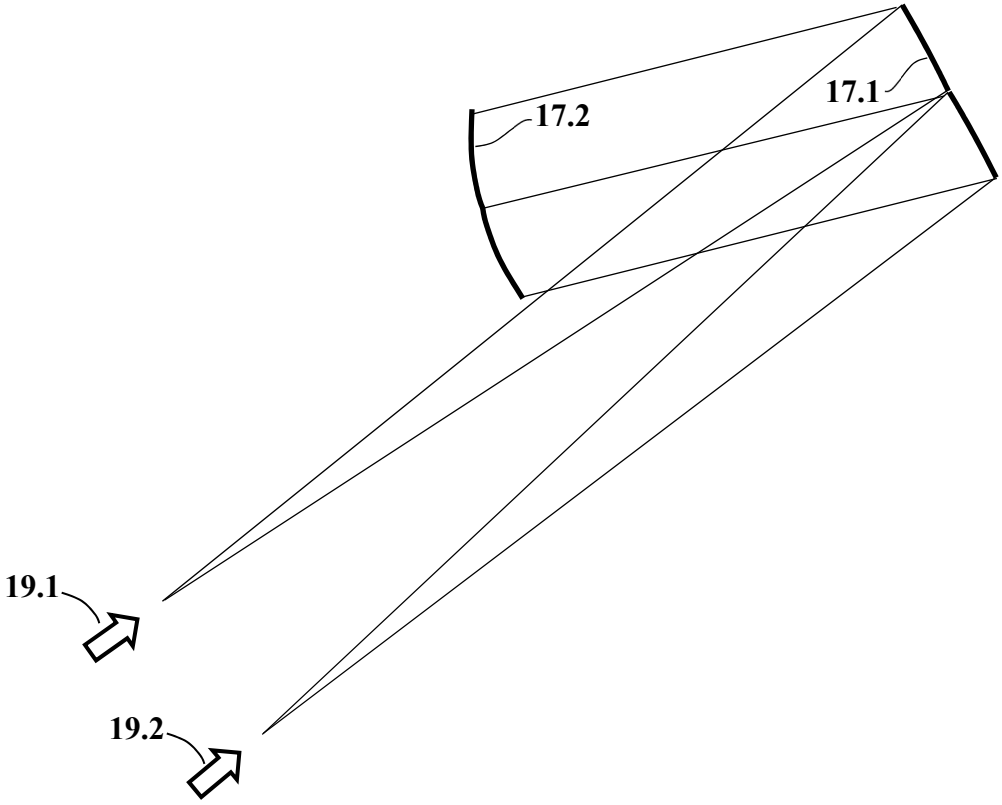

FIG. 19

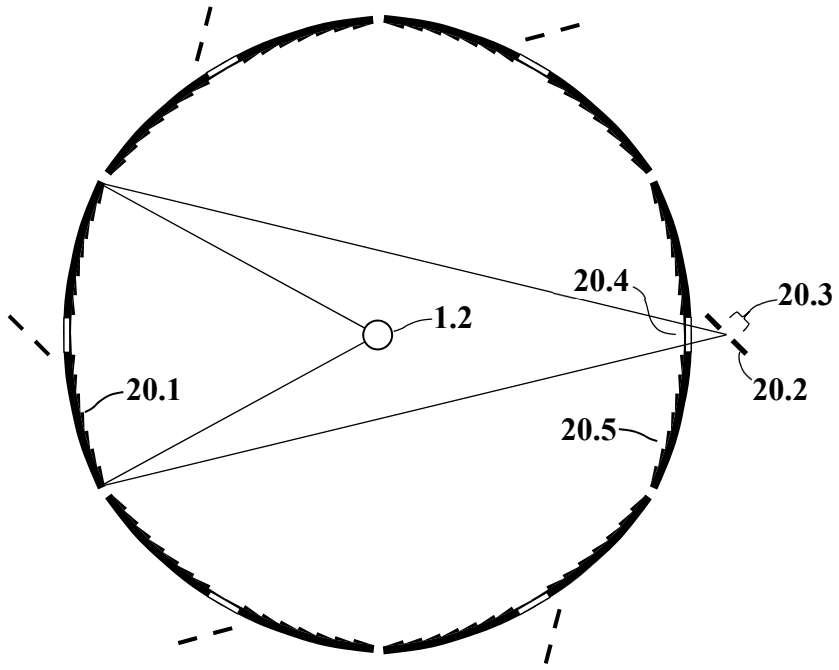

FIG. 20

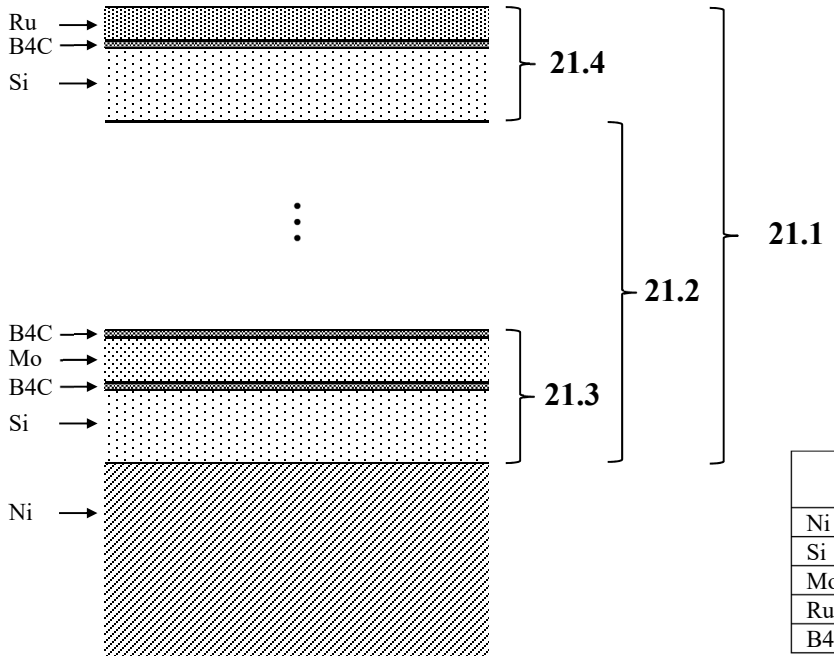

	n	Density (gm/cm^3)
Ni	0.9482+0.0727i	8.902
Si	0.9990+0.0018i	2.33
Mo	0.9238+0.0064i	10.22
Ru	0.8864+0.0171i	12.41
B4C	0.9638+0.0051i	2.52

FIG. 21

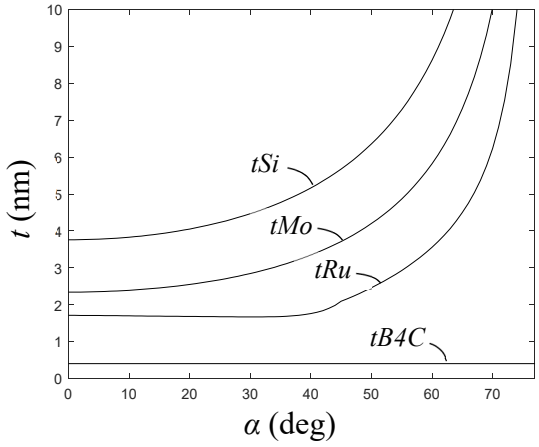

$\alpha < 77°$:

$$tSi = (13.5\text{ nm}) / \sqrt{12.9 - 15.6\sin^2\alpha + 2.22\sin^4\alpha}$$

$$tMo = (13.5\text{ nm}) / \sqrt{33.3 - 46.0\sin^2\alpha + 11.7\sin^4\alpha}$$

$$tRu = \begin{cases} (13.5\text{ nm}) / \sqrt{62.4 + 39.0\sin^2\alpha - 293.8\sin^4\alpha + 1238.5\sin^6\alpha - 1946.4\sin^8\alpha}, & \alpha \le 45° \\ (13.5\text{ nm}) / \sqrt{186.6 - 473.8\sin^2\alpha + 451.7\sin^4\alpha - 168.1\sin^6\alpha}, & \alpha > 45° \end{cases}$$

$$tB4C = 0.4\text{ nm}$$

FIG. 22

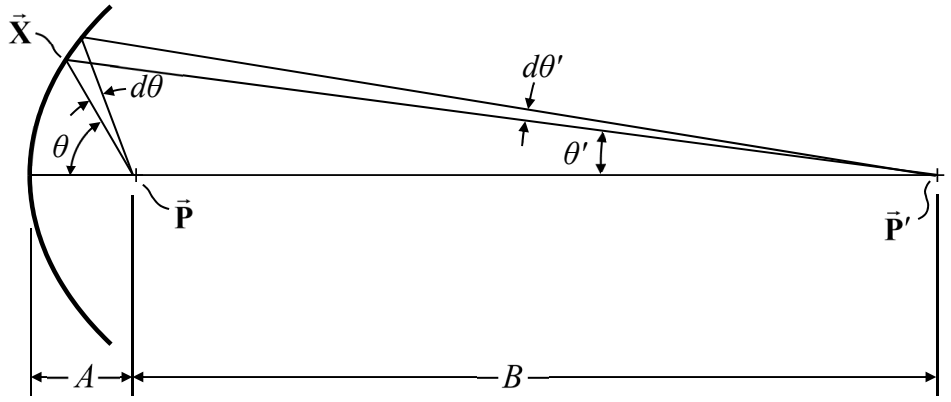
$\vec{\mathbf{X}}$
$d\theta$
$d\theta'$
θ
θ'
$\vec{\mathbf{P}}$
$\vec{\mathbf{P}}'$
A
B

FIG. 23

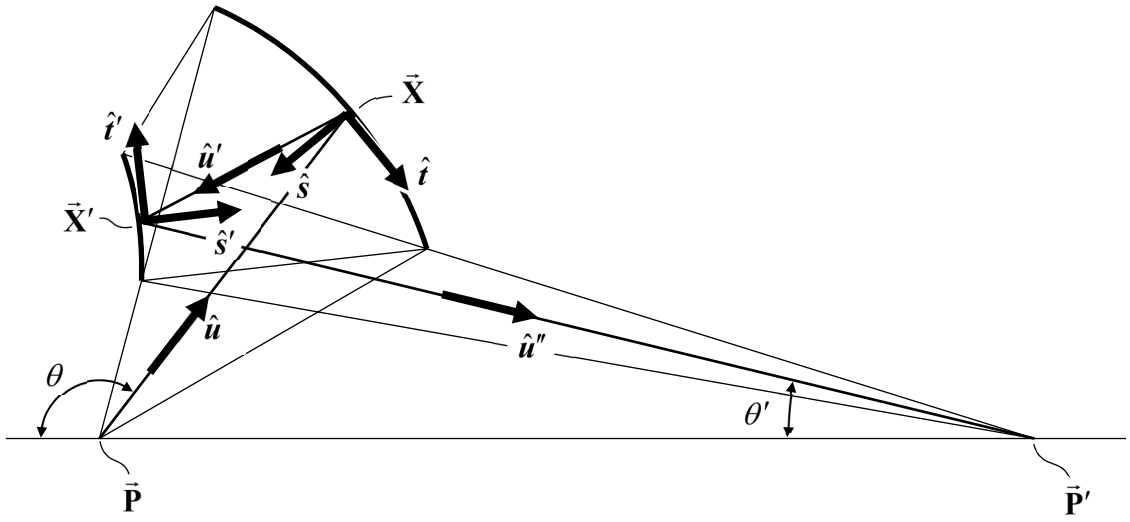
$\vec{\mathbf{X}}$
$\hat{\boldsymbol{t}}'$
$\hat{\boldsymbol{u}}'$
$\hat{\boldsymbol{s}}$
$\hat{\boldsymbol{t}}$
$\vec{\mathbf{X}}'$
$\hat{\boldsymbol{s}}'$
$\hat{\boldsymbol{u}}$
$\hat{\boldsymbol{u}}''$
θ
θ'
$\vec{\mathbf{P}}$
$\vec{\mathbf{P}}'$

FIG. 24

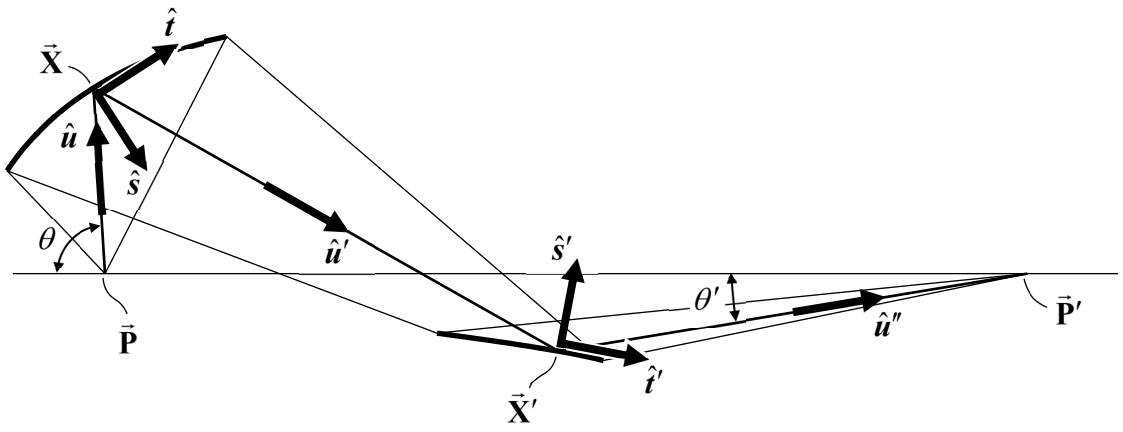
$\hat{t}$
$\vec{\mathbf{X}}$
$\hat{u}$
$\hat{s}$
θ
$\hat{u}'$
$\hat{s}'$
θ'
$\hat{u}''$
$\vec{\mathbf{P}}'$
$\vec{\mathbf{P}}$
$\hat{t}'$
$\vec{\mathbf{X}}'$

FIG. 25

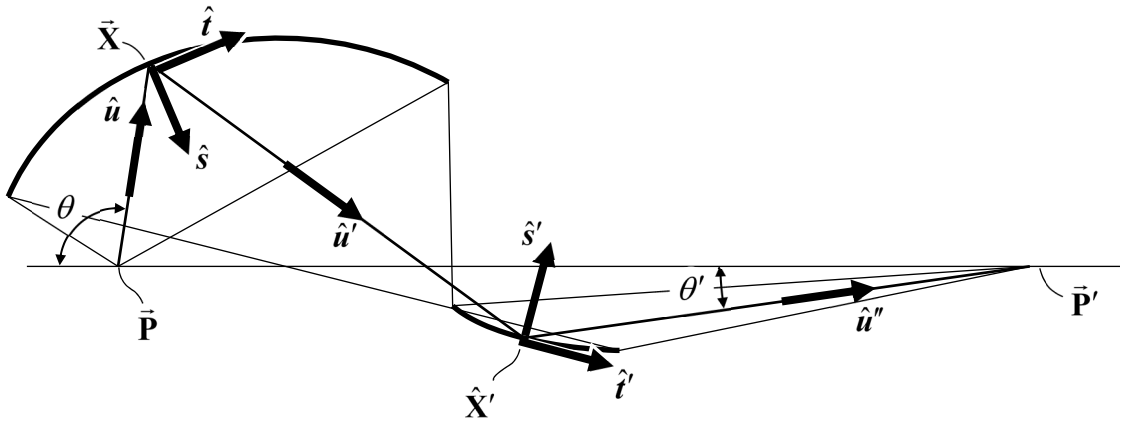
$\vec{\mathbf{X}}$
$\hat{t}$
$\hat{u}$
$\hat{s}$
θ
$\hat{u}'$
$\hat{s}'$
θ'
$\hat{u}''$
$\vec{\mathbf{P}}'$
$\vec{\mathbf{P}}$
$\hat{t}'$
$\hat{\mathbf{X}}'$

FIG. 26

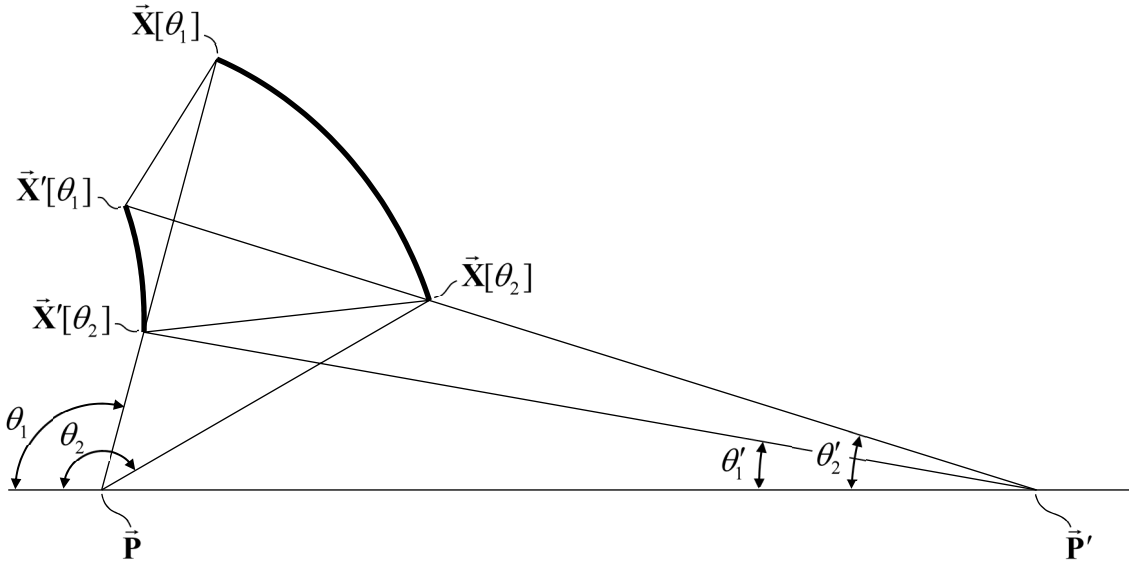
$\vec{\mathbf{X}}[\theta_1]$
$\vec{\mathbf{X}}'[\theta_1]$
$\vec{\mathbf{X}}[\theta_2]$
$\vec{\mathbf{X}}'[\theta_2]$
θ_1
θ_2
θ_1'
θ_2'
$\vec{\mathbf{P}}$
$\vec{\mathbf{P}}'$

FIG. 27

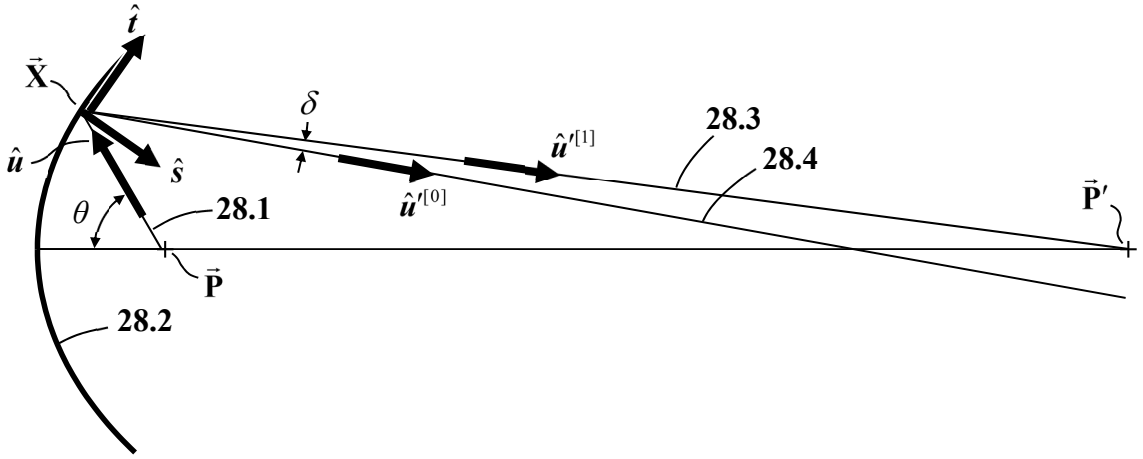
$\hat{t}$
$\vec{\mathbf{X}}$
δ
$\hat{u}$
$\hat{s}$
$\hat{u}'^{[1]}$
28.3
28.4
$\hat{u}'^{[0]}$
$\vec{\mathbf{P}}'$
θ
28.1
$\vec{\mathbf{P}}$
28.2

FIG. 28

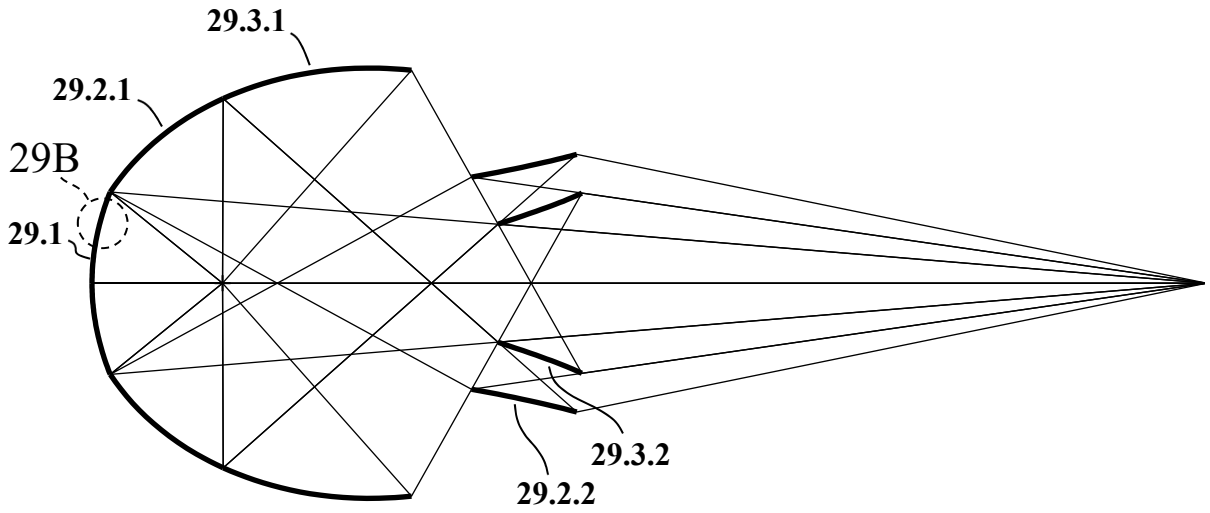

FIG. 29A

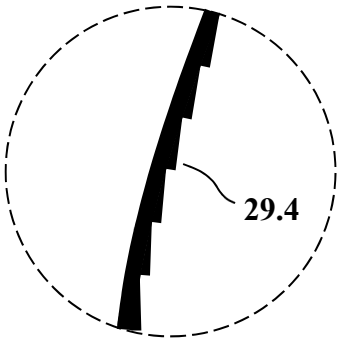

FIG. 29B

	mirror	η	I'/I	A/B	θ (deg)	θ' (deg)	α (deg)	α' (deg)
FIG. 29A	**29.1**	0.0806	53.8…40.8	0.133	0…39.00	0…4.74	0…17.13	
	29.2	0.204	40.8		39.00…90.21	8.19…11.54	5.21…24.35	71.62…63.48
	29.3	0.138	40.8		90.21…131.63	4.75…8.19	24.35…35.52	66.87…55.61
	29.1-3 total	0.422			0…131.63	0…11.54		

FIG. 30

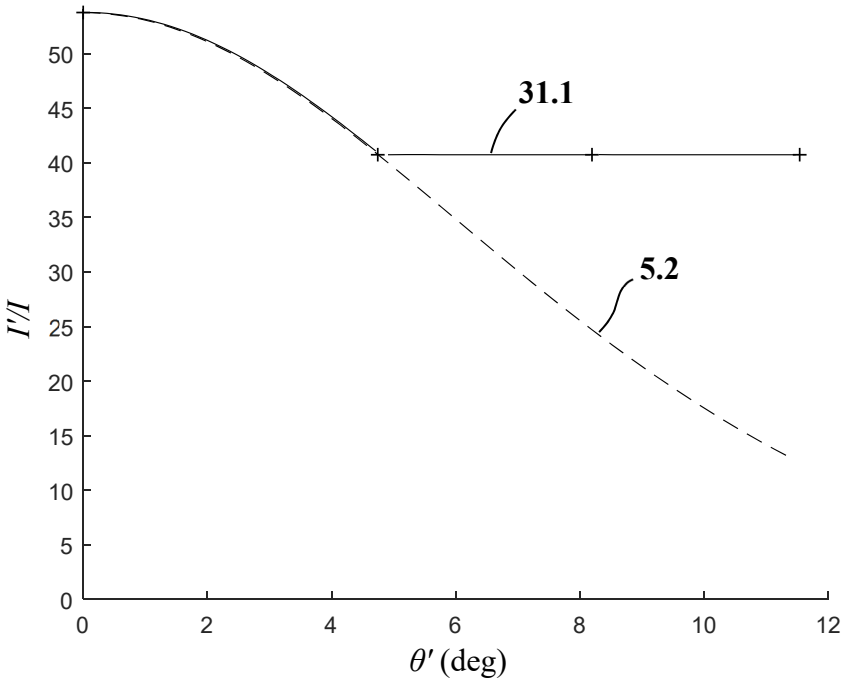

FIG. 31

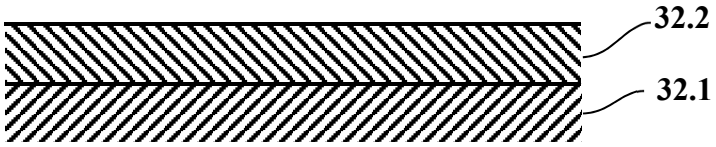

FIG. 32A

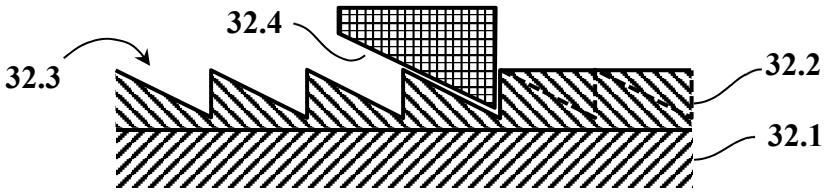

FIG. 32B

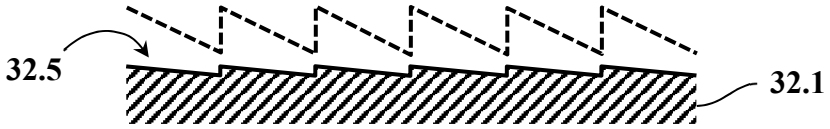

FIG. 32C

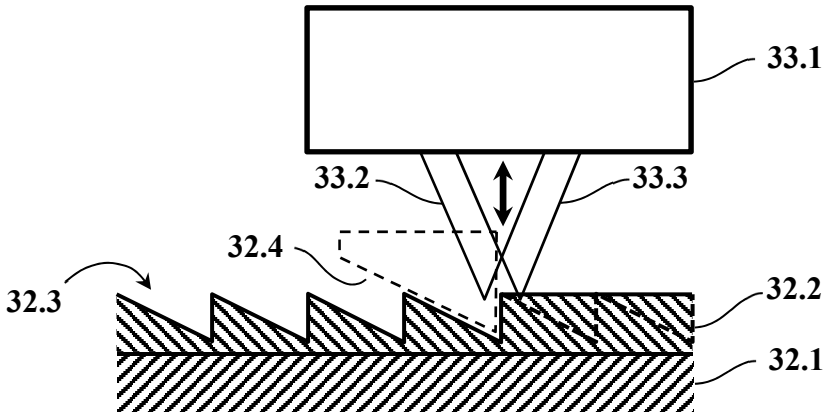

FIG. 33

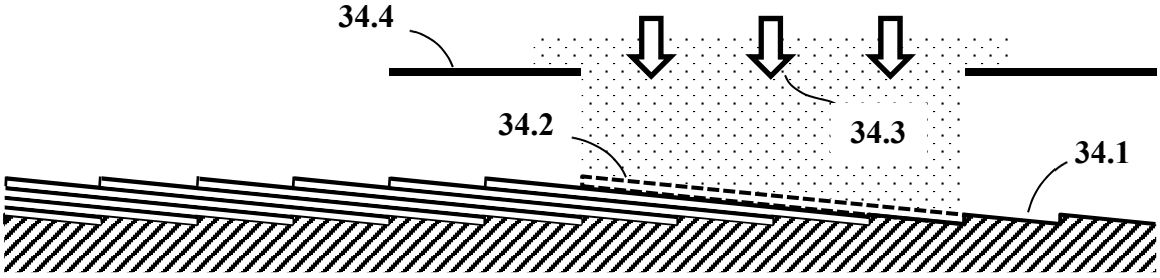

FIG. 34

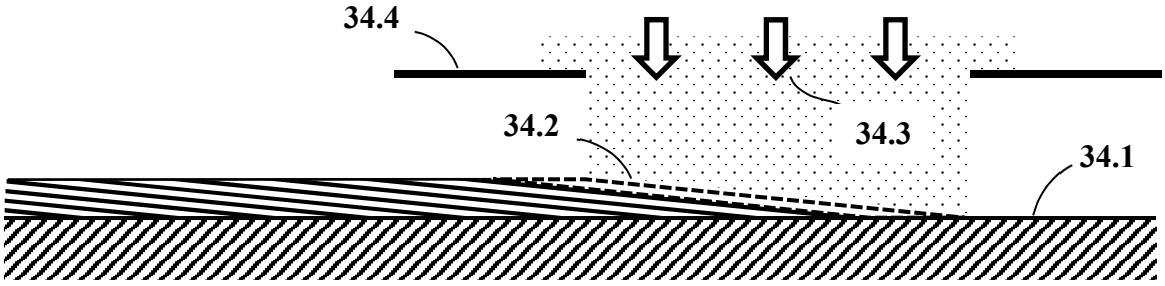

FIG. 35